Robert Meszaros BSc.

Cryogenic Electrically Detected Magnetic Resonance of Defects at the SiC-SiO_2 Interface

MASTER'S THESIS

to achieve the university degree

Diplomingenieur

Master's degree programme: Technical Physics

submitted to

Graz University of Technology

Supervisor

Univ.-Prof. Peter Hadley

Institute of Solid State Physics

Graz, November 2016

AFFIDAVIT

I declare that I have authored this thesis independently, that I have not used other than the declared sources/resources, and that I have explicitly indicated all material which has been quoted either literally or by content from the sources used. The text document uploaded to TUGRAZonline is identical to the present master‘s thesis.

Date	Signature

Contents

List of Figures

List of Tables

Abstract

Cryogenic Electrically Detected Magnetic Resonance of Defects at the $SiC - SiO_2$ Interface

by

Robert Meszaros BSc.

Institute of Solid State Physics

Graz University of Technology

Professor Peter Hadley

Wide band gap semiconductors are promising candidates for the replacement of silicon (Si) devices in power electronics and automotive applications. These materials stand out due to their large breakdown voltages. Currently industry focuses on the development of devices out of silicon carbide (SiC) and gallium nitride (GaN). SiC seems to be the most developed wide band gap material since devices are already available on the market. The development of SiC metal oxide semiconductor field effect transistors (MOSFETs) is of great interest for industry. However, the density of interface traps between the semiconductor and the oxide material in SiC devices seems to be the main disadvantage over Si devices. Due to the lattice miss match between SiC and silicon dioxide (SiO_2), point defects appear mostly at the interface of the MOSFETs. In Si MOSFETs the point defects are mainly silicon dangling bonds which can be passivated in a post oxidation annealing in a hydrogen atmosphere. Unfortunately, an annealing in a hydrogen atmosphere does not passivate the defects at the $SiC - SiO_2$ interface. Currently gases like nitric oxide (NO) or nitrous oxide (N_2O) are used for the annealing in industry. However, the passivation mechanism of these atmospheres are not fully understood since the main defects in SiC MOSFETs are not identified yet. In this work I explore the temperature dependence of paramagnetic point defects at the interface of 4H-SiC MOSFETs which were annealed with different gases. The measurements were made with electrically detected magnetic resonance (EDMR). Previous investigations found that the EDMR signal vanishes at higher temperatures. Furthermore I implemented a fairly new EDMR technique known as spin dependent charge pumping at cryogenic temperatures. In charge pumping experiments, low temperatures can be used to probe defects that are energetically situated close to the band edges. The goal was to find out if the defects close to the band edges are of a different kind. Beside SiC MOSFETs nitrogen implanted diodes were studied with EDMR. Deep level transient spectroscopy (DLTS) measurements showed that the diodes have a high concentration of the lifetime limiting defect $Z_{1/2}$. The measurements of these diodes with EDMR should have helped to identify the nature of this defect.

Kurzfassung

Cryogenic Electrically Detected Magnetic Resonance of Defects at the SiC − SiO_2 Interface

von

Robert Meszaros BSc.

Institut für Festkörperphysik

Technische Universität Graz

Professor Peter Hadley

Halbleitermaterialien mit großer Bandlücke sind vielversprechende Kandidaten um Silizium Bauteile in der Leistungselektronik und in Automobilanwendungen zu ersetzen. Diese Materialien zeichnen sich vor allem durch ihre hohe Durchbruchspannung aus. Im Moment konzentriert sich die Forschung in der Industrie hauptsächlich auf Siliziumcarbid (SiC) und Galliumnitrid (GaN). SiC ist verglichen mit GaN, weiter entwickelt, da bereits Bauteile auf dem Markt erhältlich sind. Die Entwicklung eines SiC Metall-Oxid-Halbleiter-Feldeffekttransistors (MOSFET) ist derzeit von großem Interesse für die Industrie. Die Defektdichte zwischen dem Halbleiter (SiC) und dem Oxid reicht noch nicht an den Standard heran, der bei Silizium (Si) MOSFETs erreicht wird. Aufgrund der unterschiedlichen Gitterparameter zwischen dem kristallinen SiC und dem amorphen Oxid (SiO_2) gibt es viele Punktdefekte am Grenzübergang von MOSFETs. In Si MOSFETs handelt es sich bei diesen Punktdefekten hauptsächlich um Silizium Atome mit einem ungebundenen Elektron. Diese Punktdefekte können in Si Bauteilen effizient in einer Wasserstoffatmosphäre passiviert werden. Bei SiC MOSFETs funktioniert die Passivierung in einer Wasserstoffatmosphäre nicht, weswegen andere Gase wie zum Beispiel Stickstoffmonoxid (NO) und Distickstoffmonoxid (N_2O) verwendet werden. Die Passivierungsprozesse in diesen Atmosphären sind derzeit noch Gegenstand der Forschung, da die Defekte in SiC MOSFETs noch nicht eindeutig identifiziert wurden. In dieser Arbeit wird die Temperaturabhängigkeit von paramagnetischen Punktdefekten am Grenzübergang von 4H-SiC MOSFETs, die in unterschiedlichen Gasen passiviert wurden, untersucht. Die Messungen wurden mit elektrisch detektierter Magnetresonanz (EDMR) durchgeführt. Frühere Untersuchungen derselben Bauteile zeigten, dass das Messsignal mit ansteigender Temperatur kontinuierlich kleiner wurde. Weiters wurden die Bauteile bei tiefen Temperaturen mit einer relativ neuen Methode namens Spin Dependent Charge Pumping untersucht. In herkömmlichen Charge Pumping Experimenten können bei tiefen Temperaturen Defekte, die näher bei den Bandkanten liegen, gemessen werden. Es stellte sich nun die Frage, ob diese Defekte nahe der Bandkante, sich von jenen unterscheiden, welche energetisch in der Mitte der Bandlücke liegen. Neben SiC MOSFETs wurden in dieser Arbeit auch Stickstoff implantierte Dioden gemessen. Untersuchungen mit Deep Level Transient Spectroscopy (DLTS) zeigten, dass diese Dioden über verschiedene Konzentrationen des Defektes $Z_{1/2}$ verfügen. Untersuchungen mit EDMR sollten helfen den Defekt zu identifizieren.

Acknowledgements

First I would like to thank Professor Peter Hadley for supervising this thesis and for the countless hours he spent to talk with me about semiconductor physics and the theory behind electrically detected magnetic resonance. From the institute of experimental physics I would like to thank Professor Markus Koch and Professor Ernst for letting me use the EPR/EDMR setup at their institute. I also have to thank Markus for his support with the implementation of the cryogenic EPR setup.

This work would not have been possible without the help of Gernot Gruber. He spent a lot of time teaching me the experimental skills he acquired over the years and explaining the EDMR setup he built. From Infineon Technologies Austria and KAI, I would like to thank Gregor Pobegen, Gerald Rescher and Thomas Aichinger for the support and advices they gave me in our weekly group meetings. I would also like to thank Fabian Rasinger for providing the DLTS spectra of the SiC diodes that I investigated with EDMR. Furthermore I would like to thank Josef Fugger, the head of R&D at KAI, for supporting this thesis. I would also like to thank Julia Hassler, who was doing a master thesis about EDMR investigations on hydrogen implanted silicon devices on the same setup. The countless hours we spent in the lab trying to get things running and complaining about the equipment helped to keep me sane. I also thank Martin Faccinelli for his ongoing support and his advice for programming in python.

For designing the sample holders that were needed to conduct the EDMR measurements in the microwave cavity I would like to thank Josef Friedrich from the institute of experimental physics. Furthermore I would like to thank Uwe Seidl and Martin Kornschober for building important parts of the cryogenic EPR setup in the workshop.

Chapter 1

Introduction

1.1 Motivation

The most commonly used semiconductor for electronic applications is silicon. The main advantage of silicon over the other semiconductors is the native oxide it grows. It is possible to grow an oxide on top without introducing too many defects at the interface. These defects influence the electronic properties of the devices. However, industry is interested in using other materials with larger bandgaps for power devices, which are needed in the energy and automotive sector as well as for power conversion in trains and other transportation vehicles. One promising candidate with a larger bandgap, is silicon carbide. It is the only other semiconductor with the same native oxide as silicon. The wide bandgap of silicon carbide leads to larger breakdown fields, which gives the opportunity to make the power devices smaller and operate them at higher temperatures [1]. Although silicon carbide has some major advantages over silicon, ongoing research needs to be conducted before this technology can replace silicon devices [2]. While simple devices like Schottky-Diodes or pn-diodes are already available on the market, it is currently not possible to produce transistors, which are as reliable as silicon transistors. For all devices the interface between the silicon carbide and the silicon oxide is very important for the device behaviour and reliability [3]. The defects in silicon carbide are different to those in the silicon devices and are presently poorly understood. A method for investigating these defects is Electrically Detected Magnetic Resonance (EDMR) [4].

This thesis is about EDMR measurements at cryogenic temperatures of silicon carbide power devices. These devices are nitrogen implanted diodes and lateral metal oxide semiconductor field effect transistors (MOSFETs) which were build out of SiC. For the investigations, different EDMR techniques were used. The diodes were investigated with spin dependent recombination (SDR) while the bipolar amplification effect (BAE) [5] and spin dependent charge pumping (SDCP) [6] was used to measure the MOSFETs. The thesis also investigates the influence of low temperatures on the EDMR signal.

1.2 Silicon Carbide

1.2.1 Crystal Structure

Silicon carbide consists out of bilayers of silicon and carbon atoms. They form tetrahedrons which arrange themselves into a variety of crystal structures. One carbon atom is bound to three different silicon atoms in the same layer while the fourth one lies in the layer above. Figure 1.1 shows the tetrahedral shape of silicon carbide.

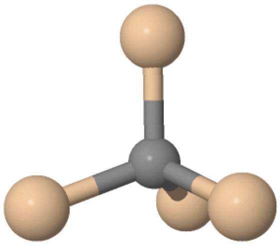

Figure 1.1: A Ball and Stick model of the tetrahedral shape of SiC with Si atoms in beige and the carbon atom in grey.

There are currently more than 150 known polytypes of silicon carbide. The orientation and the crystal structure have a high influence on properties like the bandgap and the electron mobility. The different polytypes differ in the stacking order of the tetrahedrons in the crystals unit cell. The stacking order can be explained by the model of close packed spheres, which is shown in figure 1.2. The bottom bilayer of SiC can be imagined as a sphere at position A. The bilayer above can occupy the positions B or C. The most common types are 4H-SiC, 6H-SiC and 3C-SiC. In this nomenclature the number in the front stands for the amount of stacked bilayers in a unit cell while the letter afterwards stands for the crystal lattice [1]. A comparison of the crystal structure of the different polytypes is shown in figure 1.4.

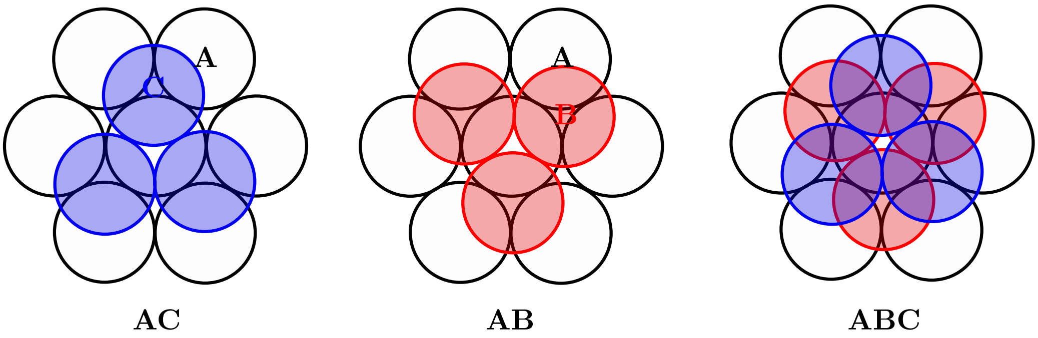

Figure 1.2: Stacking order of silicon carbide bilayers in the closed packed sphere model.

Silicon carbide has a hexagonal Bravais lattice and therefore the crystal planes are described by the Miller-Bravais indices. This notation is slightly different to the commonly used Miller indices. The directions and planes are described by the four indices h, k, i and l and are indicated in figure 1.3 as $[hkil]$. The index i is related to h and k by the following relationship.

$$i = -(h + k) \tag{1.1}$$

The direction of the surface plane is like in silicon very important for the functionality of the device. In silicon the (100) surface is used, because it grows the best oxide with the lowest defect density. For 4H-SiC the interface is grown on the (0001) plane which is perpendicular to the [0001] direction. The [0001] direction is called the c-axis.

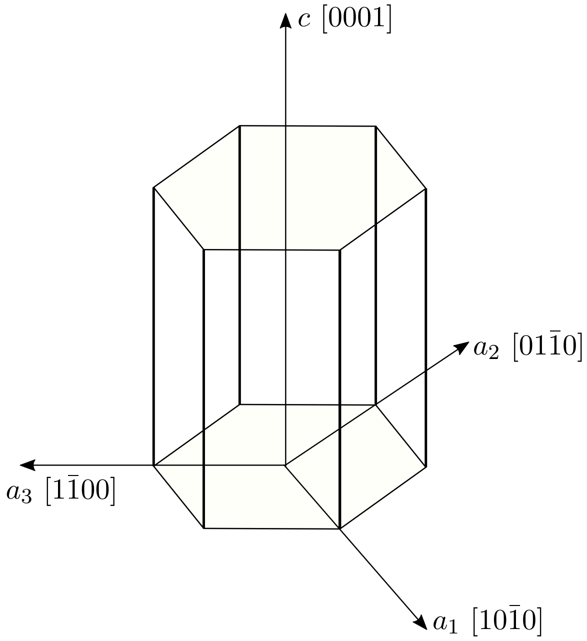

Figure 1.3: Primitive lattice vectors of the hexagonal Bravais lattice. The lattice vectors are indicated in the Miller-Bravais notation.

The most important polytypes for industry are 4H-SiC and 6H-SiC [7]. In comparison 4H-SiC has a larger bandgap than 6H-SiC. It also shows a higher and more isotropic electron mobility which makes it the preferred polytype for industrial usage [3]. The properties of the different polytypes are compared in table 1.1. 3C-SiC has a higher mobility than the other two, but is not used in industry due to its smaller bandgap. Table 1.1 shows the influence of the crystal structure on the properties of silicon carbide. Figure 1.4 shows the crystal structure of 2H-, 4H-, 6H- and 3C-SiC.

Comparing the stacking order of the different polytypes in table 1.1 and figure 1.4 one can see that 3C-SiC has a cubic symmetry. In fact it is the only known polytype with a non hexagonal symmetry. The other polytypes have a hexagonal symmetry although many of them also contain cubic sites. For instance the stacking order of an ideal 4H-SiC crystal would look like ABCB. The site C lies between two B sites and is therefore a site with a hexagonal symmetry. Site B lies between the sites A and C which gives it a cubic symmetry. Although 4H-SiC contains 50 % cubic sites its overall symmetry is hexagonal. This is discussed in more detail in [1].

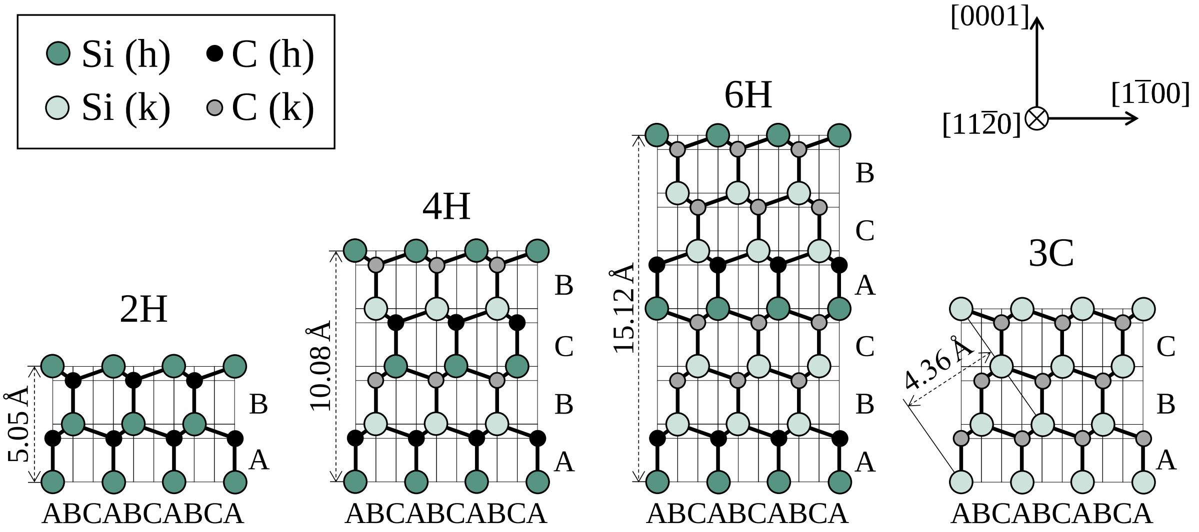

Figure 1.4: Crystal structure of 3C-SiC, 4H-SiC and 6H-SiC along the ⟨0001⟩ direction [8].

Another property of silicon carbide is its large hardness. On the Mohs scale it has a value of 9. This is due to the strong bonds that are formed between the silicon and carbon atoms. The (0001) plane mostly consists out of silicon atoms and is called the Si-face, while the (000$\bar{1}$) plane is called the C-face and therefore mostly carbon atoms are exposed on the surface [3].

Table 1.1: Comparison of the properties of the three most common polytypes.

Property	3C-SiC	4H-SiC	6H-SiC
Band gap /eV	2.39	3.26	3.0
Critical field /MV cm^{-1}	3	2.0	2.4
Saturation carrier velocity /10^{7} cm s^{-1}	2.5	2.0	2.0
Electron mobility /cm^{2} V^{-1} s^{-1}	1000	850	370
Thermal conductivity /W cm^{-1} s^{-1}	4.5	4.5	4.5
Stacking order	ABC	ABCB	ABCACB

The manufacturing of SiC wafers is completely different to the production of silicon wafers. In silicon technology a widely used method is the Czochralski process. The silicon is melted and later a seed crystal is dipped into the melt. It is pulled out slowly which causes the silicon atoms in the melt to align along the crystallographic direction of the seed crystal. The outcome is a single crystalline silicon rod which is cut into many wafers. Under atmospheric pressure and a temperature of about 2800 °C SiC goes through a peritectic phase transition which cannot be used in a Czochralski process [9]. For the industrial manufacturing of SiC wafers physical vapour transport (PVT) is used. Here a seed crystal which is held at low temperatures is placed into of a growth chamber. On the bottom of the chamber the SiC is heated up above 2800 °C under partial vacuum where it sublimates. The sublimed molecules deposit on the seed crystal and align along its crystallographic directions [1].

SiC wafers produced with the PVT method don't reach the quality of Si wafers. In order to improve the quality a homoepitaxial layer of SiC is grown on top by a chemical vapour deposition (CVD) process. This improvement of the wafer quality is crucial for device processing in industry. The potential of SiC as a semiconductor has been known for decades, but devices are still rare on the market. One of the reasons is the low yield of wafers in production. That is why the wafers are not grown with CVD directly since the growth rates are $< 5\ \mu$m/h. One major breakthrough in the last decades was to introduce step bunching into the growth process. Here the crystal is grown on a slightly off oriented (0001) axis to avoid the mixing of different polytypes during the growth process. The angle from the [0001] direction is between 3 ° – 5 ° [10, 11].

1.2.2 SiC – SiO_2 Interface

The SiC – SiO_2 interface is essential for the success of SiC in metal oxide semiconductor (MOS) technology. A lot of research has been conducted in this field. Most of what is covered in this section can be found in more detail in [3, 12]. In general all wide band gap semiconductors face four challenges for the industrial use as MOSFETs which are listed below.

- Availability of high quality epitaxial grown wafers
- Processes for doping materials n- and p-type
- Formation of ohmic contacts between the semiconductor and the metal wires
- Deposition of reliable and defect-free oxides at the interface

The last point is a major advantage of SiC over other wide band gap semiconductors. Compared to other wide band gap semiconductors the oxide that is grown on SiC yields interfaces with few defects. However the quality does not yet reach that of the Si – SiO_2 interface. The mobility of SiC at the interface of a state-of-the-art MOSFET is at least one order of magnitude smaller than the mobility in the bulk. The reason for this behaviour is yet not fully understood, however the high density of interface traps D_{it} is usually assumed to be responsible for it [13]. The different types of defects are discussed in section 1.3.

The oxide can be grown thermally or by chemical vapour deposition (CVD). In case of a thermally grown oxide the process turns out to be more complicated compared to the oxidation of silicon. In the case of silicon the oxygen has to form bonds with the silicon atoms while in SiC the carbon atoms have to be removed first from the material. The chemical reaction can be expressed as:

$$\mathrm{SiC} + {}^{3}\!/_{2}\ \mathrm{O_2} \longrightarrow \mathrm{SiO_2} + \mathrm{CO} \tag{1.2}$$

As with Si, a thermally dry or wet oxidation is possible, which is performed at about 1100°C. One major difference is the slower oxidation rate of SiC. Furthermore the oxidation of the C-face happens 5 times faster than the oxidation of the Si-face. This behaviour is not fully understood, although there are several theories [3]. One of them assumes that the oxygen binds the carbon atoms on the C-face and removes the first layer. In the second layer the carbon was bound to three silicon atoms which later can easily react with the oxygen. The three silicon atoms in the second layer are bound to one carbon atom in the third layer. On the Si-face three atoms on the surface build a strong Si-C bond with the carbon atom in the second layer. Since there is no strong driving force between the Si and the O atoms, the oxidation process is slower [14]. The main disadvantages of this method are the long oxidation time and the high temperature that is needed.

Another method for producing an oxide is chemical vapour deposition (CVD). In thermal oxidation the oxide is grown in the material by oxygen diffusing into the material, while in a CVD process it is deposited on top. Although lower temperatures are needed, the deposition of the oxide is faster compared to the thermal oxidation. Although there are different kinds of CVD processes, the basic operation mode is similar for all of them. The substrate is placed in a closed chamber which is filled by a carrier gas. The gas includes precursor molecules which are activated by temperature and/or a plasma. The precursors decompose into the favorable deposit and a volatile by-product. The by-products are pumped out of the chamber by the gas flow. There are a variety of precursor gases for depositing SiO_2. For instance in a plasma enhanced chemical vapour deposition (PECVD) process silane SiH_4 can be used as a precursor for silicon. The corresponding precursor material for oxygen is O_2, N_2O or CO_2. The process is carried out at a temperature of about 300 °C [15]. More extensive information on CVD processes can be found in [16].

The oxidation is followed by an annealing process where the wafer is placed in a certain gas atmosphere and under a specific temperature. The gas diffuses through the oxide to the interface and passivates the defects [3]. In silicon technology the interface traps are passivated with a gas mixture of nitrogen and hydrogen at a temperature between 400°C – 500°C. The hydrogen diffuses to the interface and passivates the silicon dangling bonds. In the case of SiC at the temperatures mentioned above hydrogen shows only a poor passivation of defect states, which indicates that the dominant interface traps are completely different in this material. Several gases such as H_2, O_2, N_2O and NO were used for the annealing process. Annealing processes with nitrogen containing gases are commonly used in research and industry. The state of the art annealing process is done with NO gas which enhances the reliability and performance of the resulting devices by orders of magnitudes, presumably due to the reduction of interface traps. The passivation mechanism of nitrogen is still topic of extensive research and not fully understood. Investigations with energy electron loss spectroscopy (EELS), secondary ion mass spectroscopy (SIMS) and x-ray photoemission spectroscopy (XPS) shows that nitrogen is deposited at the interface. In general NO passivates the defects better than N_2O. A model which gives a reasonable explanation suggests that N_2O decomposes under high temperature in the gas phase according to the following reactions [17]:

$$\mathrm{N_2O} \longrightarrow \mathrm{NO} + \mathrm{O} \tag{1.3}$$

$$\mathrm{N_2O} + \mathrm{O} \longrightarrow \mathrm{N_2} + \mathrm{O_2} \tag{1.4}$$

Since N_2O is the larger molecule it does not diffuse as far as the smaller O_2 and NO molecules. The oxygen atoms and molecules cause an additional oxidation since the annealing is performed under high temperatures.

1.3 Defects in SiC

In this section defects that were important for this work are briefly discussed. The dicussion will focus on intrinsic defects, which do not contain impurity atoms. Compared to silicon, there are more possibilities for the formation of intrinsic defects since silicon carbide consists out of carbon and silicon. For more information the reader is reffered to [17–19].

1.3.1 Silicon Vacancy

The silicon vacancy is a deep level defect and appears in several charge states. In irradiated SiC crystals the negative charge state $\mathrm{V}_{\mathrm{Si}}^-$ was observed with electron paramagnetic resonance (EPR). The vacancy appears in a high spin state of $S = 3/2$. The EPR spectrum yields a g-value of 2.0034 and shows a characteristic hyperfine (HF) interaction [20]. The HF interaction appears due to the natural abundance of Si and C in the material. The ^{13}C and the ^{29}Si isotopes have a nuclear spin of $I = 1/2$. The HF constants for the Si and the C atom are $a_{Si} \approx 3\ G$ and $a_C \approx 29\ G$ in case of $B \parallel c$. The $\mathrm{V}_{\mathrm{Si}}^-$ is characterized by its isotropic g-value. The HF splitting a_{Si} is also symmetric, while $a_C \approx 12\ G$ for $B \perp c$ [20]. Compared to the carbon vacancy there is no difference in the g-value for $\mathrm{V}_{\mathrm{Si}}^-$ in a hexagonal or a cubic site. The vacancy is known to be thermally stable and cannot be annealed-out below 750°C [18]. Furthermore it is known that the HF parameters for $\mathrm{V}_{\mathrm{Si}}^-$ are almost identical for the different polytypes [19]. The silicon vacancy was identified as a interface defect in SiC MOSFETs with different EDMR techniques [21]. However, recent work suggested that it is not the only paramagnetic defect at the interface [8].

1.3.2 Carbon Vacancy

The carbon vacancy appears in different charge states out of which the $\mathrm{V}_{\mathrm{C}}^+$ and the $\mathrm{V}_{\mathrm{C}}^-$ are paramagnetic and therefore can be probed with EPR. Similar to the silicon vacancy the investigation of the carbon vacancy was conducted on irradiated SiC crystals [22, 23]. Compared to $\mathrm{V}_{\mathrm{Si}}^-$ the g-value of the carbon vacancy is anisotropic [19]. The carbon vacancy shows a strong site dependence, which causes different EPR spectra for a vacancy in the cubic and the hexagonal site. The positive charged carbon vacancy $\mathrm{V}_{\mathrm{C}}^+$ was identified first and shows several HF peaks due to the ^{29}Si isotopes in the nearest neighbour shell. EPR experiments in 4H-SiC that were performed parallel and perpendicular to the c-axis yielded g-values of $g_{\parallel} = 2.0032$ and $g_{\perp} = 2.0048$ [22]. The $\mathrm{V}_{\mathrm{C}}^-$ center has a more isotropic g-value of $g_{\parallel} = 2.0040$ and $g_{\perp} = 2.0038$ at room temperature [23]. By comparing deep level transient spectroscopy measurements with low temperature EPR measurements, it was possible to assign the known carrier lifetime killing defect $\mathrm{Z}_{1/2}$ to the carbon vacancy [24].

1.3.3 Carbon Dangling Bond

A carbon dangling bond is an interface defect which was suggested at the $\mathrm{SiC} - \mathrm{SiO}_2$ interface [25]. The EPR investigations were made on a thermally grown oxide on n-type doped porous 4H-SiC. A recent study focused on EDMR at the $\mathrm{SiC} - \mathrm{SiO}_2$ interface of MOSFETs. The spectrum observed in all devices was interpreted as a carbon dangling bond at the interface. Recent density functional theory (DFT) simulations seem to be in agreement with this model. It is further known that the defect can be passivated by an NO anneal. The samples that were treated with NO showed a spectrum that was orders of magnitudes smaller [8].

1.4 Devices

There are different kinds of electronic devices available on the market like pn-diodes and metal oxide semicondutor field effect transitors (MOSFETs) which are treated in this section. They are well known devices and more extensive information can be found in any semiconductor textbook such as [26].

1.4.1 MOSFET

The MOSFET is used in high density integrated circuits and is also an important power device. In the last decades the number of transistors on a chip has doubled every two years, which is known as Moore's law. For power devices the increase of the integration density is not the first priority in industry, because they are used to switch high voltages or currents. Compared to other power devices like an insulated gate bipolar transistor (IGBT) the switching capabilities of a MOSFET are limited to voltages not higher than 1 kV. The advantage of the MOSFET as a power device is the high frequency it can be operated at.

MOSFETs are categorized according to the type of carriers in the channel. One can distinguish between n-channel and p-channel devices. The conducting channel in the n-channel devices is formed by electrons, while the p-channel is formed by holes. Furthermore the devices can be operated in enhancement and depletion mode. In enhancement mode the transistor does not conduct, when no gate voltage is applied. In depletion mode a gate bias has to be applied in order to turn off the device. For SiC power MOSFETs only n-channel type is researched due to the low mobility of holes in SiC.

A n-channel MOSFET is built on a lightly doped p-type substrate, which is called the body. On top there are two donor implanted regions which are called source and drain. They are separated by the p-type body substrate. On top there is an insulating layer of silicon dioxide with a metal contact on top, which is known as the gate. The structure of a MOSFET is shown in figure 1.5a.

By applying a positive voltage on the gate of an n-channel device a conductive channel builds up between the source and the drain region at the interface as indicated in figure 1.5b. The electron density in the channel decreases from source to drain, since the electrons near the drain get accelerated and sucked into the drain region due to the strong electric fields at the drain/body junction. The charactaristic parameters for a MOSFET are the channel length, the channel width and the oxide thickness. The channel length L describes the length between the two n^+ regions. The thickness of this conductive channel is in the order of 5 nm. For most applications the source and the body contacts are shorted. The gate electrode is made out of heavily doped polysilicon, while the source, drain and body contacts are made out of metals which form ohmic contacts with the silicon carbide surface. Especially for n-channel MOSFETs there was a lot of research conducted on ohmic contacts [17]. The type of material that is used to build an ohmic contact depends on the type of MOSFET. For n-type SiC, nickel is used for the ohmic contact formation, while for the p-type material aluminium or titanium is used. In order to form an ohmic contact with nickel, the n-region has to be heavily doped and the nickel has to be sintered at a temperature of more than 800°C [17]. The optimal thickness of the nickel layer is 50 nm $-$ 100 nm. If the thickness is too thin the contact shows a higher resistivity, while a layer that is too thick increases the surface roughness. For the metallization of p-type SiC an alloy out of aluminium and titanium is used and sintered at a temperature of 900°C. More information about the metallization of SiC can be found in [17].

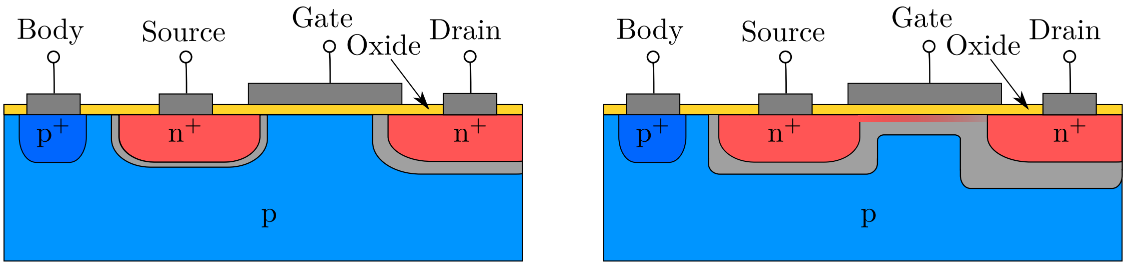

(a) MOSFET off-state (b) MOSFET on-state

Figure 1.5: Schematic diagram (a) of a MOSFET in the off-state with the n-doped regions (red), the p-doped substrate (blue), the depletion region (light grey) and the various contacts (grey). By applying a gate voltage a conductive channel builds up between the drain and source contact (b). The color gradient of the channel shows how the electron density in the channel decreases from source to drain.

The gate, the oxide and the lightly p-doped bulk semiconductor form a Metal-Oxide-Semiconductor (MOS) Capacitor. An ideal MOS capacitor is an idealized model, which does not take interface traps or oxide charges into account. The charges in the system exist in the semiconductor and on the metal surface and have opposite sign. For the following considerations the body contact is grounded and the gate is biased with a positive or negative voltage as indicated in figure 1.6a.

By changing the bias of the gate different states can exist at the semiconductor-oxide interface. These states are known as accumulation, flat band, depletion, weak inversion, threshold and strong inversion. The following discussion will concentrate on p-doped semiconductors and is therefore directly related to the n-channel MOSFET which were discussed above. The different states can be explained by energy band diagrams. Figure 1.6b shows the band diagram for a p-type semiconductor when no bias is applied. Here the Fermi level of the metal and the semiconductor are indicated as E_F and the intrinsic Fermi energy of the semiconductor is E_i. The valence band and the conduction band are indicated as E_V and E_C.

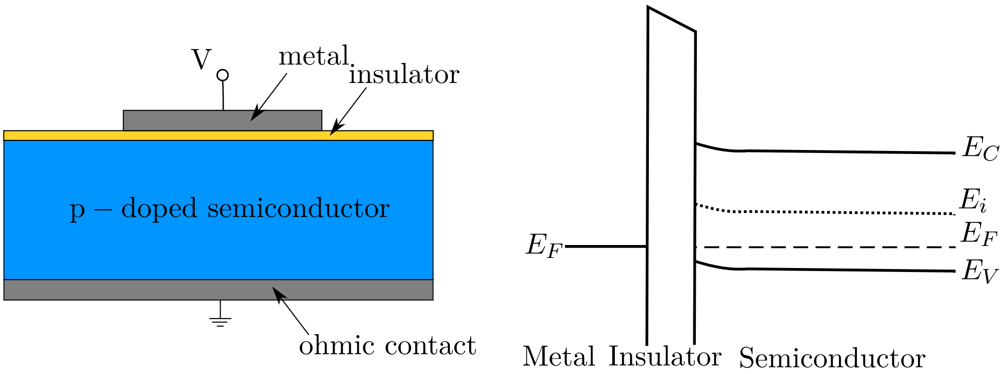

(a) MOS capacitor (b) Zero bias band diagram

Figure 1.6: Schematic diagram of a MOS capacitor (a) and its energy band diagram under zero bias conditions (b).

In case a negative bias ($V < 0$) is applied to the gate, holes are attracted to the interface. At the semiconductor-oxide interface the valence band (E_V) bends upward and is closer to the Fermi level in the semiconductor as indicated in figure 1.7a. The Fermi energy of the semiconductor remains constant under all biasing conditions. By going towards positive voltages at some point the bands are flat. The voltage that has to be applied to make the bands flat is called the flat band voltage (figure 1.7b). It is the boundary between accumulation and depletion and by applying even more positive voltages the bands will start to bend downward. By applying a higher voltage and therefore going away from the flat band voltage the interface is in depletion. There are more majority carriers (holes) than minority carriers (electrons) at the interface (figure 1.7c). At $E_F = E_i$ the number of electrons (n) is equal to the number of holes (p) at the interface. At weak inversion $E_F > E_i$ and the bands bend further so that $n > p$. This means that there are more minority carriers than majority carriers at the interface, which is indicated in figure 1.7d. In weak inversion a small current flows between source and drain which is referred to as the subthreshold current. The threshold voltage separates weak inversion from strong inversion and is an important property of MOSFETs (figure 1.7e). It is the voltage that has to be applied before the MOSFET turns on. The case of strong inversion appears when the energy difference $E_C - E_F$ at the interface equals $E_F - E_V$ in the bulk of the semiconductor (figure 1.7f).

In a MOSFET that is operated in weak inversion there are more minority carriers than majority carriers at the interface. However the carrier density is too low in order to drive a significant current from source to drain. A sufficient current flow appears at strong inversion and therefore V_{th} is considered as the threshold when the channel starts to conduct.

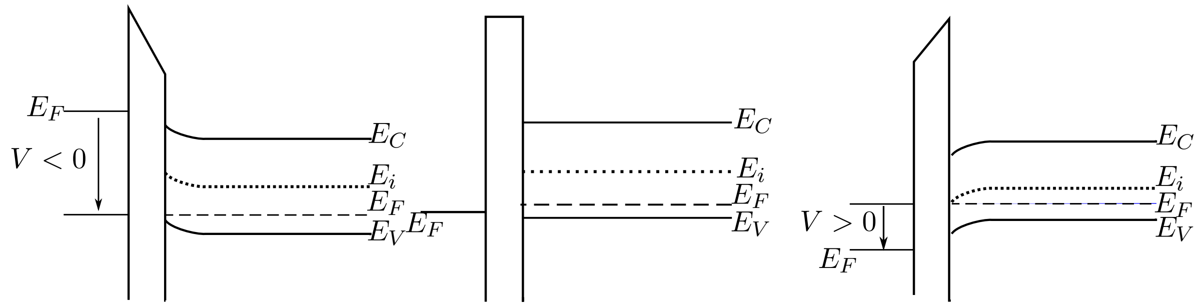

(a) accumulation (b) flat band (c) depletion

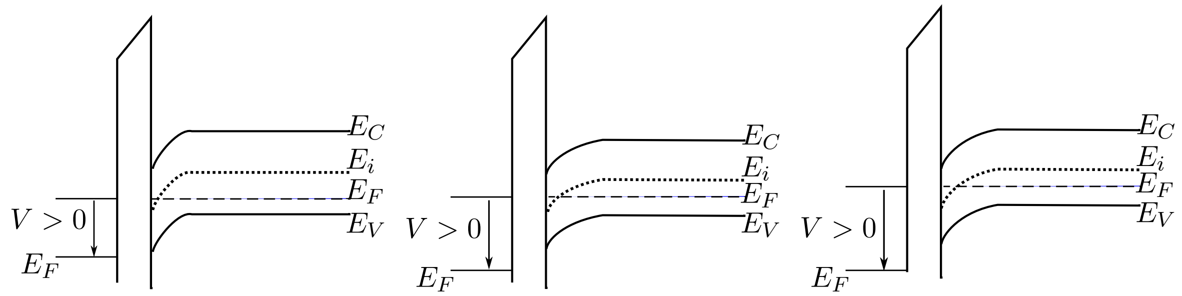

(d) weak inversion (e) threshold (f) strong inversion

Figure 1.7: Overview of the energy band diagrams for the various cases under which a MOS capacitor can be operated.

The threshold voltage V_{th} can be obtained by using

$$V_{th} = V_{fb} + 2\psi_B + \frac{\sqrt{2\epsilon_{SiC} q N_A 2\psi_B}}{C_{ox}} \tag{1.5}$$

where ϵ_{SiC} is the dielectric function of silicon carbide, q is the elementary charge, C_{ox} is the capacitance of the gate oxide and N_A is the doping concentration of the acceptors in the semiconductor. ψ_B is the body potential which depends on the difference between the Fermi energy of the doped semiconductor and the intrinsic Fermi level. The Fermi energy of a doped semiconductor is influenced by the doping concentration, the temperature T and by the intrinsic carrier concentration n_i of the semiconductor that is used.

$$\psi_B = \frac{E_i - E_F}{q} = \frac{k_B T}{q} \ln\left(\frac{N_A}{n_i}\right) \tag{1.6}$$

Equation (1.5) shows that a small threshold voltage can be reached with a large gate capacitance. The capacitance of the gate oxide depends on its dielectric constant ϵ_{ox} and the oxide thickness t_{ox}.

$$C_{ox} = \frac{\epsilon_{ox}}{t_{ox}} \tag{1.7}$$

The current-voltage characteristics of a MOSFET show how the drain current I_D depends on the gate voltage V_G and drain voltage V_D. A typical $I_D - V_D$ characteristic is shown figure 1.8. It shows that a MOSFET can be operated in three different regimes which are the linear, the nonlinear and the saturation regime. Expressions for the drain current for these three regions can be derived with the gradual channel approximation, which can be found in any semiconductor textbook like [26]. For the following discussion, the source and body are grounded while a drain voltage and gate voltage is applied.

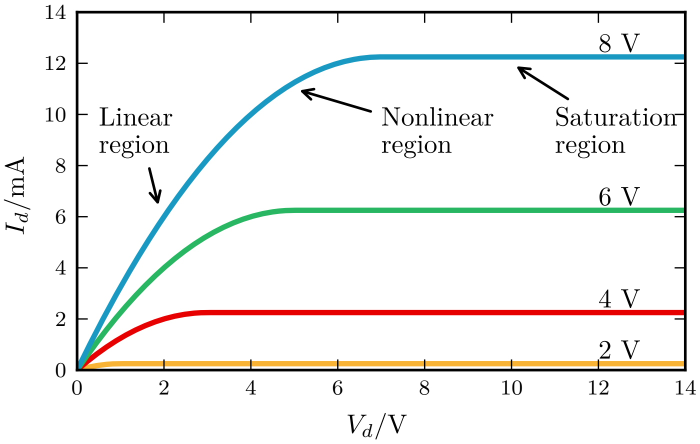

Figure 1.8: Current-Voltage characteristics of a MOSFET at different gate voltages. The three different operation regimes are indicated by arrows.

With the gradual channel approximation the following relation between the drain current and the drain voltage is obtained:

$$I_D = \frac{Z}{L}\mu_n C_{ox}\left((V_G - V_{th})V_D - \frac{V_D^2}{2}\right) \tag{1.8}$$

with Z the width of the channel, L the length of the channel and μ_n the mobility of the electrons. The linear region appears at a biasing condition of $V_D \ll V_G - V_{th}$ and the channel conducts like an ohmic resistor. For small V_D the linear terms in equation (1.8) dominates, while in the nonlinear region at $V_D < V_G - V_{th}$ the quadratic term is the dominant one. Equation (1.8) predicts a parabolic behaviour, which does not match with the curves in figure 1.8 for $V_D > V_G - V_{th}$. In fact the drain current starts to saturate at a certain drain voltage V_{Dsat}. This point is called pinch-off. Above the saturation voltage the pinch-off point shifts toward the source region in the MOSFET. The area between the pinch-off point and the drain region is fully depleted. The saturation current I_{sat} can be expressed as:

$$I_{sat} = \frac{Z}{2L}\mu_n C_{ox}(V_G - V_{th})^2 \tag{1.9}$$

Defects and impurities in the crystal lattice of a MOSFET were not considered in the derivation above. The mobility μ_n is an important parameter of a MOSFET and is influenced by scattering effects. Impurities are partly responsible for the scattering of charge carriers in a semiconductor. There are several different scattering mechanisms present at the same time. Every mechanism can be associated with a certain mobility (μ_i). The total mobility (μ_{tot}) can be calculated with Mathiessen's rule

$$\frac{1}{\mu_{tot}} = \sum_i \frac{1}{\mu_i} \tag{1.10}$$

A high density of interface traps (D_{it}) limits the mobility in a MOSFET device. Furthermore charge carriers can be trapped by the defects at the interface and therefore reduce the carrier lifetime. By charging traps in the oxide, the threshold voltage of the devices can be shifted which would alter the current-voltage characteristics of the device (figure 1.8). The shift in threshold voltage (ΔV_{th}) can be calculated by

$$\Delta V_{th} = \frac{1}{\epsilon_{SiO_2}} \int_0^{t_{ox}} x\rho_{ox}(x)dx \tag{1.11}$$

where ϵ_{SiO_2} is the dielectric constant of the oxide, x is the depth of the oxide and $\rho_{ox}(x)$ is the density of the trapped charges in the oxide. The degradation of the mobility and the shift of the threshold voltage due to the defects at the interface and in the oxide are major issues in SiC device fabrication.

1.4.2 SiC Diodes

In power device applications, SiC diodes are used for power switching. They conduct large currents with low losses in the on-state and block high voltages with low leakage in the off-state. Figure 1.9 shows the schematic diagram of a SiC diode. It consists out of two heavily doped p and n-regions that are separated by a lightly doped n-region. Due to the thick lightly doped region the device can block high voltages in reverse bias. For more detailed information about SiC diodes as power devices the reader is referred to [17].

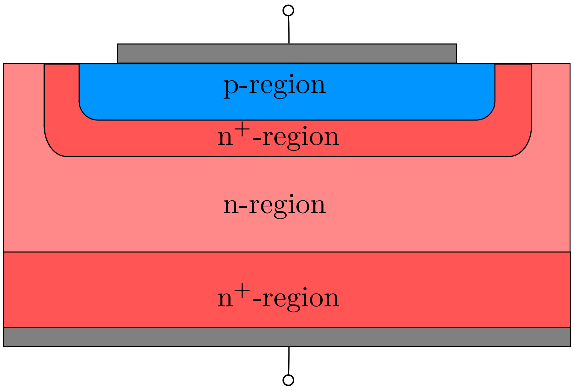

Figure 1.9: Schematic diagram of a SiC diode. A small region of the device was heavily implanted with aluminium (p$^+$-region). The heavily (n$^+$) and lightly (n) doped regions were implanted with nitrogen. The metal contacts are indicated in grey.

Note that during the experiments the diodes are slightly forward biased and their full potential as a power device is not used. Especially the defects in the heavily nitrogen implanted device give a strong EDMR signal. For this reason the diode is used as a standard in order to show that the cryogenic setup is comparable to other X-band measurements and to investigate the effects of cryogenic temperatures on the measurement signal. The current through the device can be described by

$$I = I_S \cdot \left(\exp\left(\frac{eV}{nk_BT} \right) - 1 \right) \tag{1.12}$$

where I_S is the saturation current, e is the elemental charge, V is the voltage across the diode, n is the non-ideality factor, k_B is the Boltzmann constant and T is the temperature. The saturation current I_S of a diode is strongly temperature dependent and is described by

$$I_S = Aen_i^2 \left(\frac{D_p}{L_pN_D} + \frac{D_n}{L_nN_A} \right) \tag{1.13}$$

where A is the cross sectional area, D_p and D_n are the diffusion coefficients for holes and electrons, respectively, while L_p and L_n are the diffusion lengths for holes and electrons. N_D and N_A are the doping concentrations for donors and acceptors. The diffusion coefficients also show a temperature dependence which is given by

$$D_p = \frac{\mu_p k_B T}{e} \qquad D_n = \frac{\mu_n k_B T}{e} \tag{1.14}$$

where μ_p and μ_n is the mobility of the holes and the electrons respectively. The temperature dependence of the intrinsic carrier concentration is given by

$$n_i = \sqrt{N_C N_V} \exp\left(\frac{-E_g}{2k_B T}\right) \tag{1.15}$$

$$E_g = E_g(T=0) - \frac{\alpha T^2}{T+\beta} \tag{1.16}$$

where E_g is the band gap of the semiconductor and α and β are material constants. For silicon carbide $\alpha = 8.2 \cdot 10^{-4}$ eV/K and $\beta = 1.8 \cdot 10^3$ K [17]. N_C and N_V are the effective density of states for the conduction and the valence band respectively. At room temperature they have values of $N_C = 1.8 \cdot 10^{19}$ cm^{-3} and $N_V = 2.1 \cdot 10^{19}$ cm^{-3} [17]. The following equations can be used to calculate the effective density of states for the conduction and valence band for different temperatures.

$$N_C(T) = N_C(T = 300\ K)\left(\frac{T}{300}\right)^{3/2} \tag{1.17}$$

$$N_V(T) = N_V(T = 300\ K)\left(\frac{T}{300}\right)^{3/2} \tag{1.18}$$

The equations above show that the temperature strongly influences the IV-characteristics of a diode. This behaviour is important for performing measurements at low temperatures.

1.5 Electron Spin Resonance

Electron spin resonance (ESR) also called electron paramagnetic resonance (EPR) is a widely used method to investigate paramagnetic point defects in solid materials. The first measurements were performed in 1945 by Zavoisky. The defects can be charaterized by their g-value and by the hyperfine interaction of the electrons with the nuclei that possess a spin. The explanation in this section will focus on continous wave (CW) EPR. Today there are many textbooks about EPR such as [27, 28] which cover most of what is written in this section. Further developments of ESR led to a variety of EDMR methods like BAE and SDCP which are covered in the following chapters.

1.5.1 Paramagnetism

Since EPR is limited to the investigation of paramagnetic defects, a brief explanation is necessary. A substance is considered to be paramagnetic when it consists out of atoms, ions or electrons which have a permanent magnetic dipole. By applying an external magnetic field the spins align along the direction of the field. This means that the magnetic field in the material is stronger than outside. An electron in a magnetic field has a magnetic spin moment $\mu_{\mathbf{S}}$, which is given by

$$\mu_{\mathbf{S}} = -g_e \mu_B \mathbf{S} \tag{1.19}$$

where g_e is the g-factor of a free electron, μ_B is the Bohr magneton and $\mathbf{S}$ is the spin angular momentum. In case the electron is bound in an orbital state it also has a orbital magnetic moment $\mu_{\mathbf{L}}$ which is given by

$$\mu_{\mathbf{L}} = -\mu_B \mathbf{L} \tag{1.20}$$

where $\mathbf{L}$ is the orbital angular momentum. The total magnetic moment is given by $\mu_{\mathbf{tot}} = \mu_{\mathbf{S}} + \mu_{\mathbf{L}}$. A defect in a semiconductor that has an unbound electron can be considered as paramagnetic. For this reason the method is widely used in semiconductor research.

1.5.2 Spin Hamiltonian

The interaction of electrons with an external magnetic field is given by the standard spin Hamiltonian. For the purpose of this thesis the spin Hamiltonian can be expressed as

$$\mathcal{H} = \mathcal{H}_{\mathcal{Z}} + \mathcal{H}_{\mathcal{HF}} = \mu_B \mathbf{S} \cdot \mathbf{g} \cdot \mathbf{B_0} + \sum_i \mathbf{A}_i \cdot \mathbf{I}_i \cdot \mathbf{S} \tag{1.21}$$

where the first term includes the electron Zeeman interaction and the second term includes the hyperfine interaction between electrons and nuclei with a spin $I > 0$. $\mathbf{B_0}$ is the magnetic field and $\mathbf{g}$ is a second rank tensor. The electron spin operator is given by $\mathbf{S}$. $\mathbf{A}_i$ and $\mathbf{I}_i$ represent the hyperfine constant and the nuclear spin operator of the i-th nucleus. For a detailed description about the spin hamiltonian the reader is referred to [28].

1.5.3 Zeeman Splitting

An electron can be characterized by its spin which in case of a single electron is $S = 1/2$. By applying a magnetic field B_0 the spin can be aligned parallel or anti-parallel to the external field which corresponds to $m_s = +1/2$ and $m_s = -1/2$. These two states are often referred to as spin up and spin down. The difference in energy of the two states is given by the Zeeman Splitting. In thermal equilibrium a higher amount of states with the lower Zeeman energy are occupied. At zero magnetic field all spin orientations have the same energy and are called degenerate. It is possible to induce transitions between the two Zeeman levels by applying an oscillating magnetic field B_1 perpendicular to the external magnetic field B_0 with the exact same energy as the splitting. The condition for resonance is given by

$$h\nu = g\mu_B B_0 \tag{1.22}$$

were h is Planck's constant, ν is the frequency of the resonance field B_1, g is the g-factor, μ_B is the Bohr magneton and B_0 is the external magnetic field that is applied. The induced transitions cause an equal distribution of states in both Zeeman levels. The time the system needs to restore the initial condition can be described by the time constant T_1 which is known as the spin-lattice relaxation time. B_1 is applied as an electromagnetic wave inside a microwave resonator where the sample is situated. The cavity is designed so that the electric component of the electromagnetic wave (microwave) is zero at the sample's position. Next to the external magnetic field every sample has an additional local field. These two add up an build an effective magnetic field. The variable g-value takes the local magnetic fields into account. For this reason the g-factor differs for different materials although it is close to the one of the free electron. Since every paramagnetic defect has another g-value, it can be used to characterize it. In the first term of equation (1.21) the g-value is indicated as a tensor and depends on the orientation to the magnetic field. By measuring the g-value for different orientations to the magnetic field the tensor elements can be determined. The values can be compared to ab-initio simulations in order to identify the defect. A more detailed description of the ESR method and the setup can be found in section 1.5.5. Equation (1.22) shows that, for a field of 3000 G the resonance will appear at a frequency of 9 GHz. This frequency lies in the so called X-Band (8 GHz – 12 GHz) and is widely used in ESR measurements.

1.5.4 Hyperfine Interaction

The hyperfine interaction occurs when the magnetic moment of the unbound defect electron interacts with a nucleus that has a magnetic moment and is in close proximity to the defect electron. The Hamiltonian of the hyperfine interaction is part of the spin Hamiltonian in equation (1.21). Since the hyperfine interaction depends on the nuclear spins in the close proximity of the defect electron, it contains information about the chemical composition near the defect. Silicon and carbon have a natural abundance, which means that a fraction of all silicon and carbon atoms will appear as isotopes which have a nuclear spin. Table 1.2 shows the nuclear spins of the isotopes which are important in this thesis.

Table 1.2: Nuclear spin I and natural abundance N for several elements which are important in this thesis.

Isotope	I	N /%
^{29}Si	1/2	4.67
^{13}C	1/2	1.11
^{14}N	1	99.63

1.5.5 EPR Method and Measurement

A basic ESR setup consists out of several magnets and a microwave source in order to establish resonance conditions. Most of the spectrometers are operated at constant frequencies while the magnetic field is swept. The measurement signal is processed by different electronic instruments which measure the signal and log the data on a computer. A schematic diagram of a basic EPR setup is shown in figure 1.10.

The sample is placed in the resonator cavity which is connected to the microwave bridge. The microwave source of common EPR setups is usually operated in the X-Band at a frequency of 9.4 GHz. When the condition for resonance is fulfilled, microwaves are absorbed by the sample. The microwaves are partly reflected out of the cavity and are measured by the detector. The static field is produced by an electromagnet which needs to be very stable since a change in the magnetic field would cause fluctuations in the energy separation. This would lead to a broadened line width in the spectrum. A second magnet is used to sweep the magnetic field. At a certain field and a fixed frequency the resonance condition is fulfilled which means that microwaves are partly absorbed and the detector measures a change in the intensity. The signal in ESR experiments is small compared to the noise. For this reason a Lock-In amplifier is used which can measure small AC signals. These amplifiers are able to perform accurate measurements even when the noise is orders of magnitude higher than the signal itself. It uses a technique called phase sensitive detection in order to filter an AC signal of known frequency and phase. Therefore it compares the signal with a reference signal. Since the diode is detecting a DC signal an additional magnetic field is used to modulate the signal. This is done by the modulation coils which are integrated in the cavity. The modulation is done with the reference signal of the Lock-In amplifier. This detection method yields the derivative of the absorption spectrum of the investigated sample. More extensive information about Lock-In detection can be found in [29].

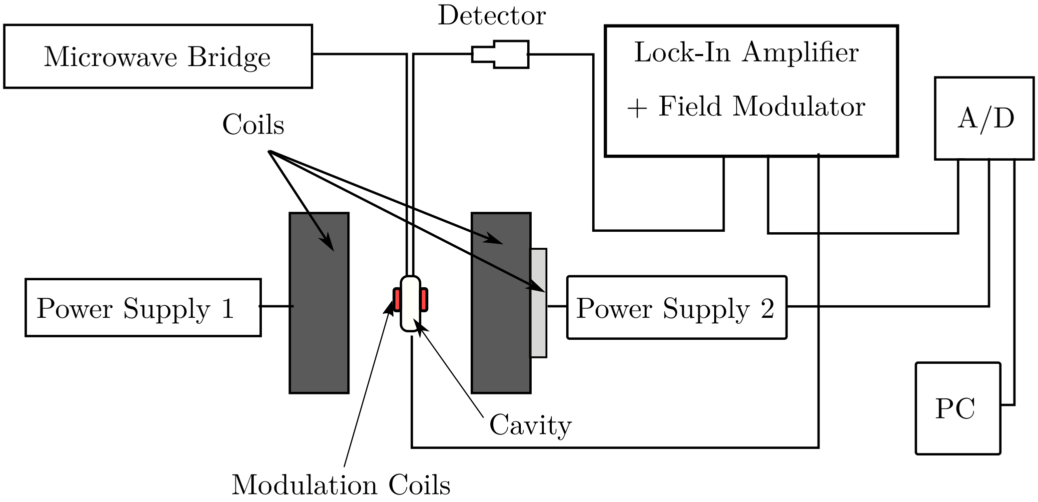

Figure 1.10: Schematic diagram of a EPR setup. Here the magnetic coils for the static magnetic field are dark grey, the magnets for sweeping the field are light grey and the coils for the modulation are indicated in red. Power supply 1 is used to drive the static magnetic field while power supply 2 is used to sweep the magnetic field during the measurement.

Chapter 2

Cryogenic EPR/EDMR Setup

2.1 X-Band Setup

In this work a low temperature X-band EPR setup was used to perform the measurements. The system is shown in figure 2.1. For the generation of the microwave field an HP 8672A Synthesized Signal Generator was used. For EPR measurements the absorption signal was detected by a diode and processed by a lock-in amplifier (SR830) as described in section 1.5.5. The sample was placed in a double resonator Varian cavity which was connected to a dewar by double-walled glass pipes. In order to ensure a good thermal insulation the space between the glass walls was evacuated. On top of the cavity an adapter was built in the workshop (figure 2.3). It was designed to avoid problems with the freezing of the electrical contacts on the PCB circuit board which was used as a sample holder for the EDMR measurements. For monitoring the temperature, a Pt100 temperature sensor was placed inside the glass pipe that led through the microwave cavity.

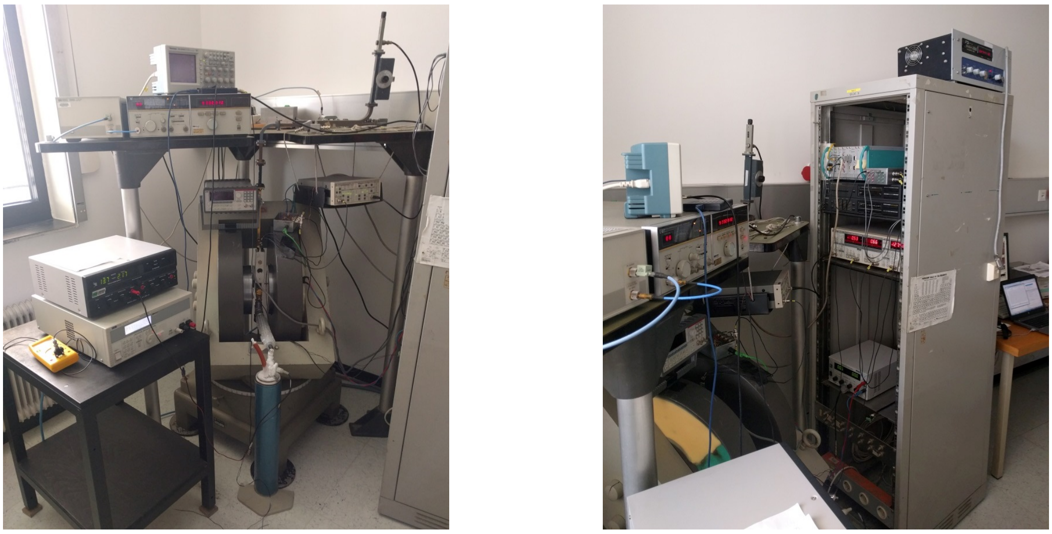

Figure 2.1: Continous wave EPR setup with a double resonator cavity and an X-band microwave source. On the left picture the magnet, the microwave bridge, the dewar and two power supplies are shown. On the right picture there is the lock-in amplifier, the magnetometer and an analog-to-digital converter on the rack.

The cooling circuit consisted out of a dewar filled with liquid nitrogen (LN_2). Load resistors with a series resistance of 6.8 Ω at room temperature were placed inside the dewar and were heated in order to evaporate the nitrogen. The cold nitrogen gas flew through the pipes to the cavity and cooled down the sample. A certain gas flow had to be maintained to keep the devices at a constant temperature. The gas flow was controlled by the power supply that heated the resistors in the dewar. For the operation at low temperatures, a higher bias had to be applied to the resistors. Figure 2.2 shows how the temperature depends on the power dissipated in the resistor. Furthermore it shows that the limitation of the cooling system is about −120°C. In practice it was possible to reach temperatures down to −160°C however it was not possible to keep the temperature stable since the high pressure caused leakage at the connection of the pipes and the dewars outlet. Since lower temperatures required a higher gas flow, the duration of the measurement at such a low temperature was shortened due to the limited amount of LN_2 in the dewar. The Pt100 sensor was read out over the computer with a TinkerForge PTC Bricklet which consisted out of a MAX31865 resistance-to-digital converter. The module has a 15 bit temperature resolution. For measurements a 2-wire Pt100 sensor was used.

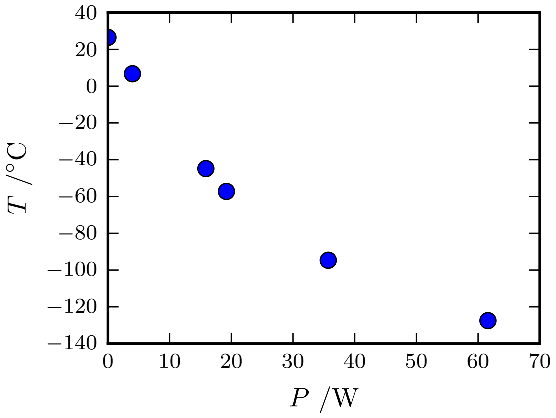

Figure 2.2: Characterization of the temperature inside the cavity as a function of the load on the resistors in the dewar. The minimum temperature that could be reached under stable conditions was −120 °C.

The double-walled glass pipe that goes through the cavity was stabilized by a Teflon plug which was mounted with an aluminium thread on top of the cavity. In order to avoid freezing of the cavity and the contacts of the sample holders, an aluminium adapter was added on top of the cavity. It was connected over a fitting to the aluminium thread. The fitting between the thread and the aluminium was made out of Teflon for a good thermal insulation. The aluminium construction was designed with a small outlet pipe in the front and a steel cylinder on top. The cylinder had a 7 mm hole in the middle and a 2 mm broad slit across the surface. Furthermore a brass screw was mounted in the front of the aluminium block in order to fix the steel cylinder. The cylinder was used to tilt and fix the PCB sample holders. The built-in construction is shown in figure 2.3. The CAD plans and a 3D model of the construction and the cavity can be found in appendix A.

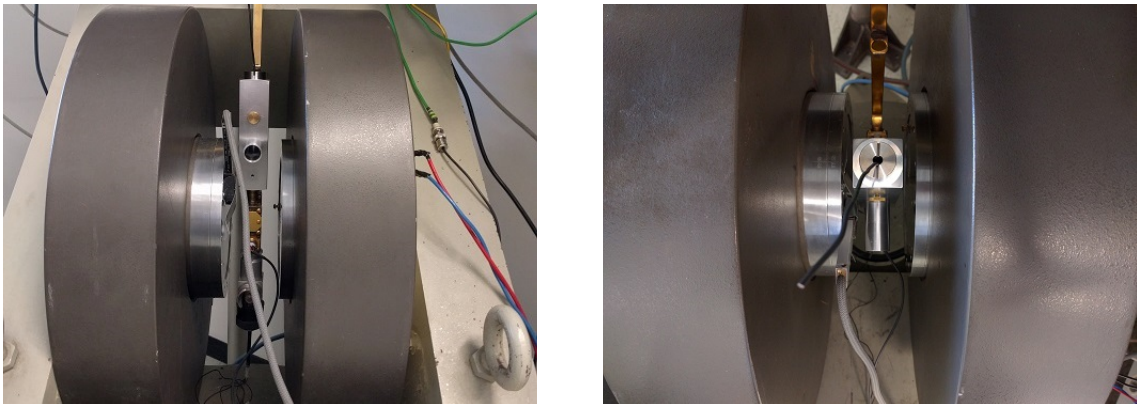

(a) Front view (b) Top view

Figure 2.3: (a) shows the front view of the aluminium construction with the brass screw and the outlet pipe. (b) shows the steel cylinder with the 7 mm hole and the 2 mm slit from the top.

As described in section 1.5.5, the internal reference signal of the lock-in amplifier is used to modulate the signal by generating a field in the modulation coils which are located on each side of the cavity. In EPR and EDMR experiments, the modulation is chosen so that it is smaller than the linewidth of the spectrum. A bigger amplitude causes a broadening of the spectrum, but it also reduces the noise and increases the signals intensity. The settings on the lock-in amplifier can be used to change the amplitude of the AC voltage which drives the oscillating magnetic field B_1. The corresponding AC current at the output was measured by a multimeter. In order to determine the current that corresponds to a modulation amplitude of 1 G the broadening of the linewidth of a spectrum was measured as a function of the modulation current. Therefore several EPR spectra of the paramagnetic substance 2,2-diphenyl-1-picrylhydrazyl (DPPH) were measured at different modulation currents as shown in figure 2.4a. DPPH is a chemical compound that is composed out of stable organic radicals. In EPR measurements it shows a strong signal and is therefore used as a standard for the position of the spectrum since it has a well known g-value of 2.0036. The distance between the minimum and maximum value $\Delta \mathrm{B}_{\mathrm{pp}}$ of each spectrum was measured and plotted as a function of the modulation current (figure 2.4b). The data was fit with a line in order to determine the slope which has the unit of $\frac{\mathrm{G}}{\mathrm{mA}}$. The inverse slope gives the amount of AC current that corresponds to a modulation amplitude of 1 G. For the cavity used, the inverse slope had a value of 11 $\frac{\mathrm{G}}{\mathrm{mA}}$.

The magnets in the setup were driven with constant current power supplies while the magnetic field was measured by a NMR standard placed in the magnetic field. However the magnetic field at the NMR standard and the one at the sample is not the same. The difference in the magnetic field causes a g-value that is different to the known one. For this reason the position of the spectrum is shifted so that the measurement yields the correct g-value. Figure 2.5 shows a DPPH spectrum without the correction and a green marker that indicates where the resonance of the spectrum should be to give the known g-value. The resonance of the measured spectrum and the known value of DPPH are 0.3 G apart. This shows that a small difference in the magnetic field would yield two different g-values. This is important for later described EDMR measurements where the g-factor is used to identify the defect. For this reason a DPPH calibration measurement is performed before every EDMR measurement.

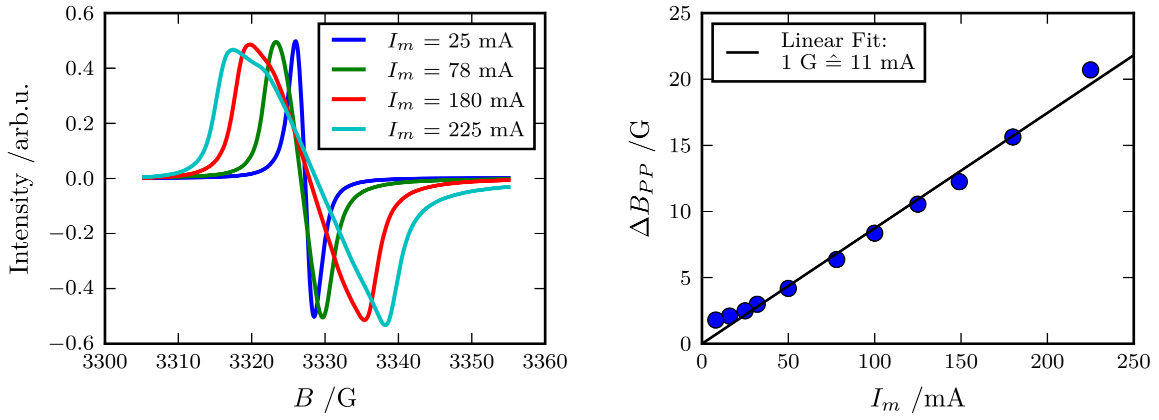

(a) DPPH measurement (b) Calibration

Figure 2.4: Calibration of the modulation coils for a frequency of 900 Hz. DPPH was measured at different modulation amplitudes (a). The distance between maximum and minimum in terms of magnetic field of each spectrum was measured and plotted as a function of the modulation current (b). The inverse slope of a linear fit yielded the current that equals a modulation amplitude of 1 G.

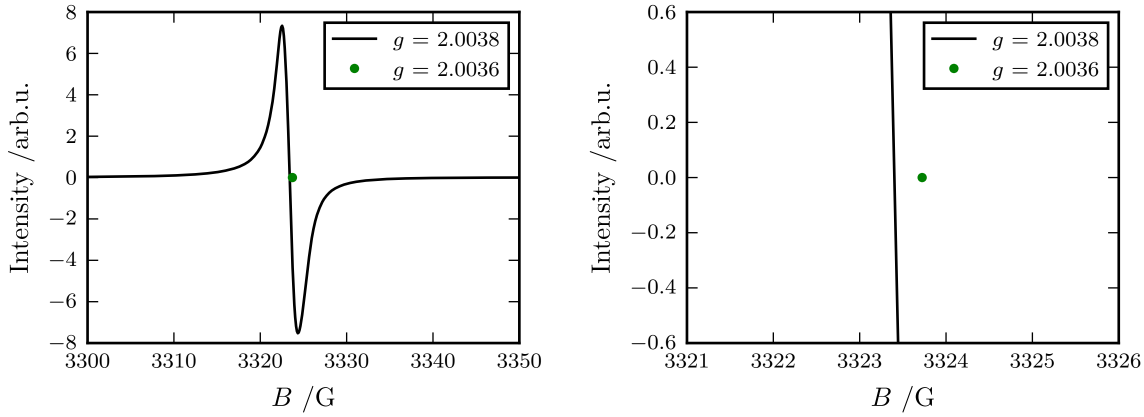

(a) DPPH spectrum (b) Enlarged spectrum

Figure 2.5: EPR spectrum of DPPH with a g-value of 2.0038 (a). The deviation of the measured value to the theoretical value is about 0.3 G (b). The green marker shows where the resonance should occur in order to yield a g-factor of 2.0036.

2.2 Sample Holder

The sample holder was a printed circuit board (PCB) that consisted of a composite material and is reinforced by fibreglass. There were four gold plated copper traces for electrical measurements. This made it suitable for building connections with wire bonds. With the four traces it was possible to connect the drain, source, body and gate contact of a MOSFET to the circuit board. The device and the bonds were covered in a gel which worked as a protective layer since the bond wires are sensitive to mechanical stress. The PCB circuit board was 4 mm wide and 25 cm long. An image of the sample holder is shown in figure 2.6. Figure 2.7 shows a nitrogen implanted pn-diode bonded to the PCB. The CAD plans of the specimen holder can be found in appendix A.

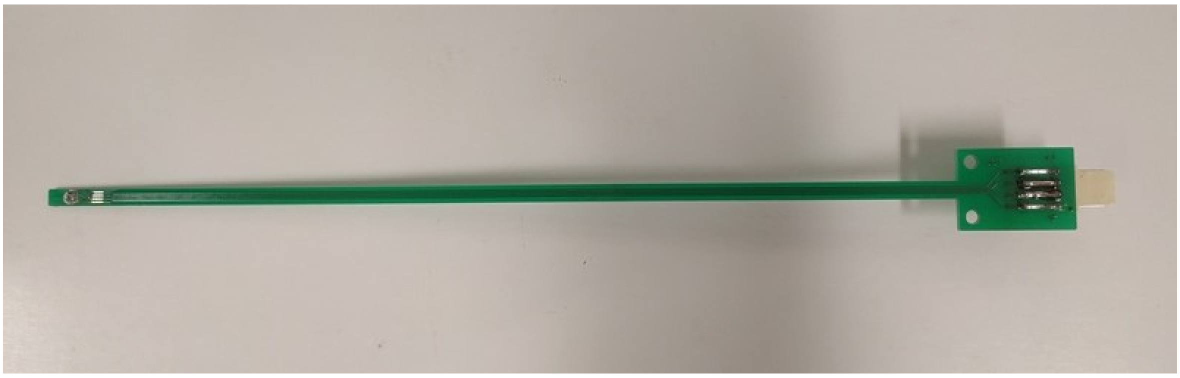

Figure 2.6: Image of the sample holder where the devices were bonded on. The device is situated on the end thin tail at the left side of the image.

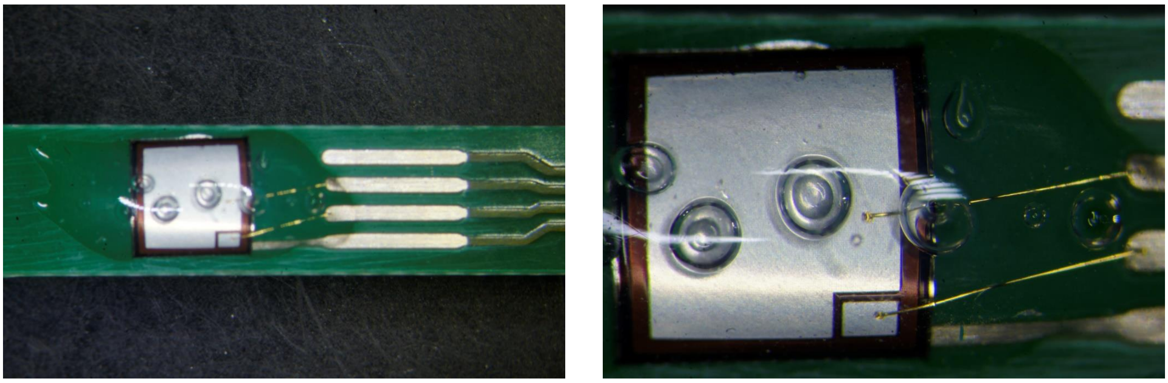

(a) PCB sample holder

(b) Diode with wire bonds

Figure 2.7: (a) shows a pn-diode bonded to the metal traces of the sampleholder. The copper traces were plated with bonding gold to ensure a good electrical connection between the device and the circuitry. (b) shows how the two contacts of the diode are connected to the sampleholder via the bonds. The device and the bonds are coverd by a gel for protection.

2.3 Nitrogen Implanted Diode

In order to test the X-band setup described in section 2.1, a nitrogen implanted diode with known g-value and signal shape was measured. The device was biased between the p-region and the n-region and was known to give a strong EDMR signal. The EDMR measurement was obtained in the nonlinear region at a forward bias of 2.15 V with a microwave power of 0 dBm. In this region recombination dominates over diffusion which causes a strong change in current under resonance condition. Since the N implanted diode yields a strong EDMR signal, the modulation amplitude was set to 1 G at a modulation frequency of 900 Hz. The signal was averaged over 180 sweeps to reduce the noise. The data was compared to a measurement of the same device at another setup. Both diodes yield the same g-value which is shown in figure 2.8a. The signal of all measurements were normalized in order to compare the hyperfine interaction. The shape of the EDMR signals are identical which indicates that the sample holder and setup works as expected. Recent studies of a similar device compared the experimental results with extensive density functional theory simulations. They suggest that the defect is a nitrogen atom situated at a carbon site paired with a silicon vacancy (N_CV_{Si}) and measured a g-value of 2.0054 parallel to the c-axis [30]. However, in the investigated device a g-value of 2.0044 was found. The obtained spectrum was compared with the one of the N_CV_{Si} defect which is illustrated in figure 2.8b. The spectrum of [30] shows a different g-value, but a similar hyperfine structure. The latter suggests that the observed spectrum is the one of the N_CV_{Si}. The linewidth of the spectrum is broader than the one obtained with the N implanted diode that was investigated in this thesis. A reasonable explanation could be that the spectrum in [30] was conducted at a higher microwave power. However, it is unclear why the g-value shifts. More information about the theory and the experimental details of EDMR can be found in chapter 3.

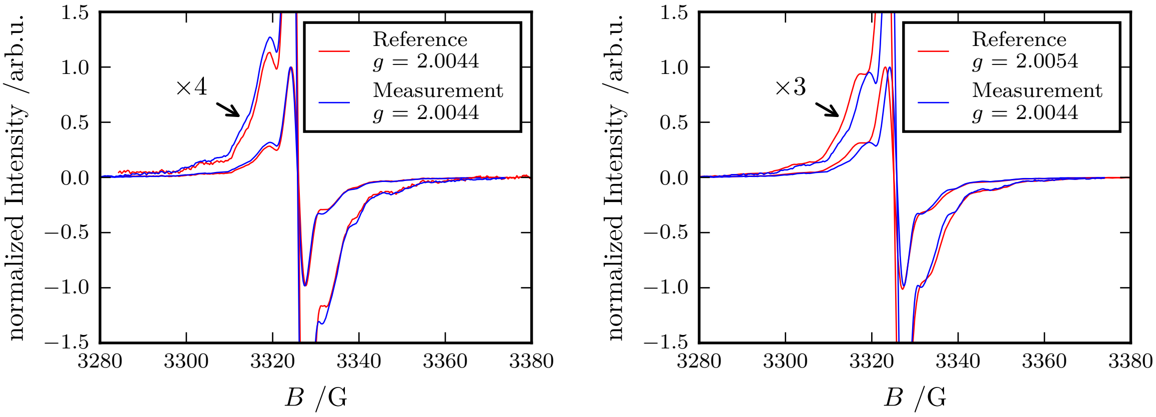

(a) EDMR signal on two different X-band setups (b) Comparison of the N implanted diode with [30]

Figure 2.8: (a) shows the normalized EDMR signal of an N implanted diode. The measurement was compared to a reference signal of the same device that was obtained at another X-band setup. (b) shows the obtained EDMR spectrum in comparison with the data of the N_CV_{Si} defect out of [30].

Table 2.1: Measurement parameters of the EDMR spectra of the N implanted diode which were obtained at different temperatures.

T /°C	ν /MHz	V_B /V	I /μA
30	9333.390	2.130	2.2
0	9334.468	2.265	2.4
-65	9335.630	2.520	2.2
-120	9336.460	2.710	2.0

In order to test the cryogenic setup, the diode was measured at low temperatures. Figure 2.9a shows how the IV-characteristics changes as a function of temperature. The measurement conditions of the EDMR spectra in figure 2.9b are listed in table 2.1.

The shift of the resonance frequency is caused by the thermal contraction of the cavity due to the low temperature. The EDMR spectra were recorded at a modulation amplitude of 1 G. The signal was averaged over 5 sweeps to improve the signal to noise (SNR) ratio. The sensitivity of the preamplifier and of the lock-in amplifier was set to 100 nA/V and 500 μV/V respectively. These settings are explained in more detail in section 3.2. The IV-characteristics (figure 2.9a) show that under constant biasing conditions the current decreases with decreasing temperature. This behaviour is theoretically described by equation (1.12). The shift of the forward bias at cryogenic temperatures had to be considered for recording the EDMR spectra. At constant biasing conditions the current value at low temperatures was too small to measure a reasonable change in current under resonance conditions.

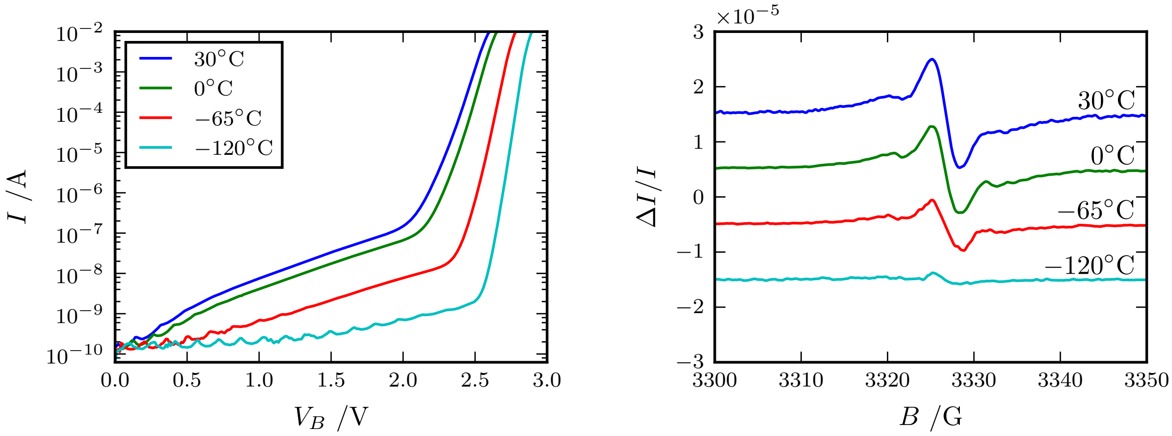

(a) IV characteristics

(b) EDMR signal

Figure 2.9: (a) shows the IV-characteristics of the diode inside the microwave cavity at a power of 0 dBm as a function of temperature. (b) shows the temperature dependence of the relative EDMR signal of the N implanted diode. In order to compare the signals at different temperatures the spectra were arbitrarily shifted.

For this reason the voltage was increased to get a current of approximately 2 μA at each temperature step (table 2.1). The low temperature spectra (figure 2.9b) show approximately the same noise level while the relative signal decreases for lower temperature. A reason could be that the operating point, where the maximum value of $\Delta I/I$ is obtained, changes with temperature. Figure 2.10a shows the relative EDMR signal for several temperatures under different biasing conditions. Here the relative signal is approximated with the difference between the maximum and the minimum value of the peak. The shift of the EDMR signals in terms of the bias voltage V_B (figure 2.10a) is explained by the temperature dependence of the IV-characteristics which can be seen in figure 2.9a. For lower temperatures a higher bias voltage has to be applied. The EDMR spectra in figure 2.9b were all recorded at a similar current which is listed in table 2.1. Under these biasing conditions the EDMR signal shows the highest relative signal change at 0°C. In order to measure EDMR signals with a similar value of $\Delta I/I$ for lower temperatures, the biasing conditions have to be adjusted since the operating point has changed. Figure 2.10b shows how the relative signal at different temperatures depends on the current. Furthermore figure 2.10 shows that for low temperatures the relative signal decreases in general.

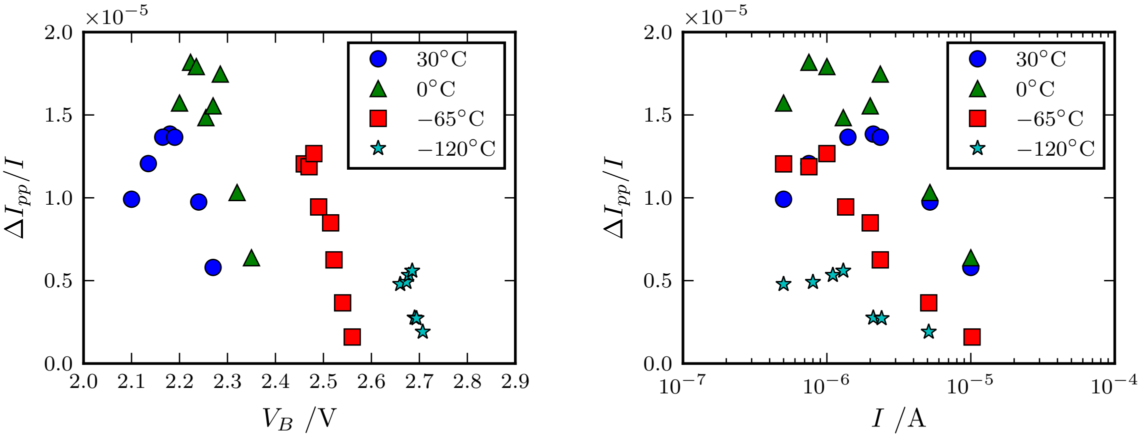

(a) Relative signal as a function of V_B

(b) Relative signal as a function of I

Figure 2.10: Relative EDMR signal of the N implanted diode at different temperatures and under different biasing conditions. (a) shows the relative signal as a function of the biasing voltage while (b) shows it as a function of the current.

Chapter 3

Electrically Detected Magnetic Resonance (EDMR)

This chapter focuses on the investigation of SiC MOSFETs with electrically detected magnetic resonance. EDMR is a modification of the widely used EPR method which was discussed in section 1.5. While EPR faces a detection limit of about 10^{10} total spins in a system, the EDMR method is orders of magnitude more sensitive [31]. Instead of measuring the microwave absorption through transitions between the Zeeman levels, EDMR detects a change in the conductivity caused by a recombination processes. In EPR the sensitivity is limited by the Zeeman splitting and the detection sensitivity of the diode, which detects the absorbed microwaves. The high sensitivity of EDMR is explained by the higher accuracy that can be reached with current measurements [4]. Since the samples in semiconductor technology have usually less than 10^{10} defects, EDMR is a commonly used method to investigate the defects in semiconductor devices such as a MOSFET [32]. The region of the device that can be probed with EDMR can be influenced by applying different biasing conditions, which affect the thickness of the depletion region. Recombination processes are observed within the depletion region since the concentration of electrons and holes are in the same order of magnitude.

3.1 Spin Dependent Transport Mechanisms

In order to understand EDMR it is important to discuss how the current in a semiconductor depends on the spin. In general there are three possibilities how the spin of an electron or hole can influence the transport through the semiconductor. These are spin-dependent scattering, spin-dependent tunnelling and spin-dependent recombination. In all of the three spin dependent transport mechanisms there are at least two spins involved which include the electron or hole in the conduction or valence band and a paramagnetic defect center. In EDMR measurements of semiconductor devices, the dominating transport mechanism is spin-dependent recombination (SDR). For this reason the following explanation will focus on this effect. For more information on tunnelling and scattering the reader is referred to [4].

3.1.1 Lepine Model

The recombination process in a semiconductor often involves a defect center that is energetically located in the bandgap. The first model for a spin dependent change in conductivity was

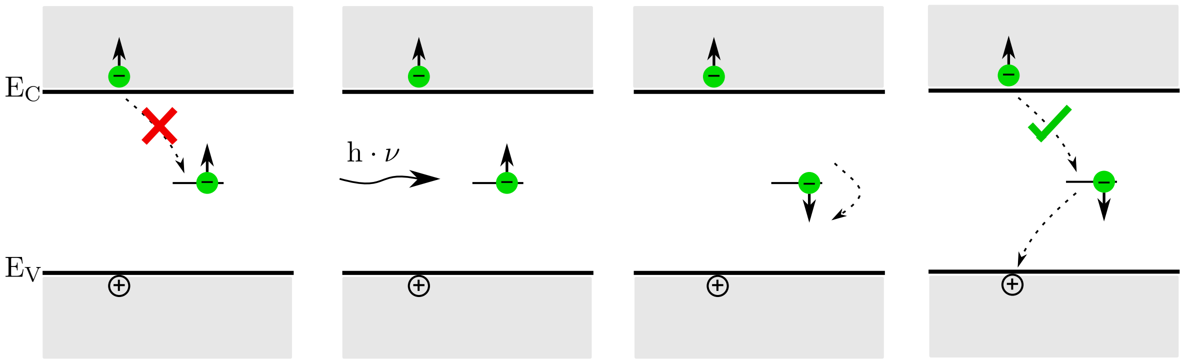

Figure 3.1: Schematic diagram of the spin dependent recombination process during the EDMR measurement. The picture on the left shows a forbidden recombination of two electrons with the same spin due to the Pauli exclusion principle. The two images in the middle show how the spin of the defect center is flipped by a microwave photon. Due to the spin flip the recombination of the electrons are allowed, which is shown in the image on the right.

introduced by Lepine [33]. The model combines the Shockley-Read-Hall (SRH) [34] model for recombination and the Pauli exclusion principle. By applying an external magnetic field, the spins can be aligned parallel or anti-parallel. If the spin of the electron and the paramagnetic defect is aligned parallel to each other, a transition is forbidden due to the Pauli exclusion principle. In the case that the two spins are aligned anti-parallel, the transition is allowed. When the resonance condition (equation (1.22)) is satisfied, one of the two spins is flipped by the microwave photon and the transition is allowed. Figure 3.1 shows how the Lepine model describes the spin dependent recombination. Lepine's work described the change in photoconductivity due to recombination of photocarriers with silicon surface states in a Si crystal. For the relative signal $\frac{\Delta\sigma}{\sigma}$ his model yields

$$\frac{\Delta\sigma}{\sigma} \leq \left(\frac{h\nu_0}{2k_BT}\right)^2 \tag{3.1}$$

were h is Planck's constant, ν_0 is the microwave frequency, k_B is the Boltzmann constant and T is the temperature. For a temperature of 300 K and under X-band radiation the relative signal change yields $6 \cdot 10^{-7}$ [4]. This value does not agree with the experimental results where the relative change of the conductivity is orders of magnitude larger than the theoretical value. Although equation (3.1) predicts a temperature and frequency dependence of the signal, experimental results show that there is only a small dependence on these two quantities [4].

3.1.2 Kaplan-Solomon-Mott Model

A better explanation is given by the Kaplan-Solomon-Mott (KSM) model [35] which takes the coupling of both spins into account. The model describes an electron in the conduction band that gets trapped by a defect, which is energetically situated in the band gap. The electron gets trapped independently of the spin orientations of the defect electron and conduction band electron. Furthermore the model uses the fact that the spin orbit coupling in materials like silicon and silicon carbide is weak, which means that the two electrons either form a singlet or a triplet state. The normalized states are

$$|s\rangle = \frac{1}{\sqrt{2}}(|\uparrow\downarrow\rangle - |\downarrow\uparrow\rangle) \qquad |T_1\rangle = \frac{1}{\sqrt{2}}(|\uparrow\downarrow\rangle + |\downarrow\uparrow\rangle) \qquad |T_2\rangle = |\uparrow\uparrow\rangle \qquad |T_3\rangle = |\downarrow\downarrow\rangle \tag{3.2}$$

where s is the singlet state and $T_1 - T_3$ are the triplet states. The singlet and the triplet states differ in energy. The total spin of the singlet state is $S = 0$, while the triplet states have a total spin of $S = 1$. This means that the triplet state can appear in the substates $\mathrm{m_s} = -1, 0, +1$.

For any recombination process the spin angular momentum has to be conserved. For this reason only the singlet states are allowed to recombine. In equilibrium the probability that two electrons build a singlet or a triplet state is $^1/_4$ and $^3/_4$ respectively. However, due to the conservation of angular momentum the singlet states are allowed to recombine and therefore the population of singlet states decreases. After a certain time a steady-state is reached, where the population of the triplets is much higher than the singlet population. Microwaves can flip either the spin of the electron or the hole, when resonance occurs. This way triplets can be converted into singlets and vice versa. Figure 3.2 shows that only the singlet states are allowed to recombine. A full theoretical description of the KSM model is out of the scope of this thesis and can be found in [36].

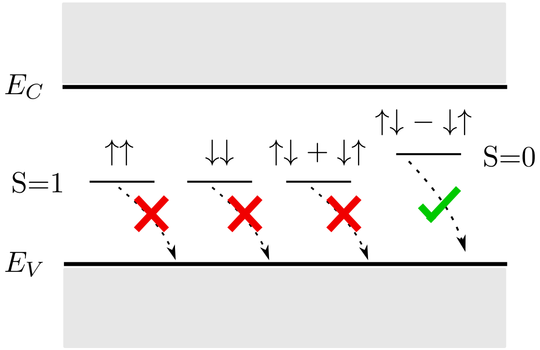

Figure 3.2: The figure shows that recombination processes over singlet states (S = 0) are allowed, while the ones over triplet states (S = 1) are forbidden.

3.2 EDMR Setup

The EDMR setup is slightly different to the EPR setup which was described in section 2.1. Instead of detecting the absorption of microwaves in the sample, EDMR records a change in the current due to an enhancement of recombination processes in the semiconductor under resonance conditions. The device under investigation is bonded on a sample holder as described in section 2.2 and placed inside the microwave resonator. In order to observe recombination processes as described in section 3.1 there have to be electrons, defects and holes in the probed region of the device. For this reason the devices have to be biased. The various EDMR methods that were used in this thesis differ in the biasing conditions of the device, which will be explained in the following sections. Compared to EPR the EDMR method shows orders of magnitude higher sensitivity since current measurements can be made more accurately than microwave absorption measurements. As in EPR, the lock-in detection technique is used to detect the signal. The lock-in amplifier compares the measurement signal with a reference signal. A brief introduction into the lock-in detection technique can be found in section 1.5.5 and for more extensive information the reader is referred to [29]. For this work a SR830 lock-in detector was used. It acts like a band-pass filter with a time constant of 300 ms and a slope of 24 dB/decade. Since the lock-in amplifier only has a voltage input the current that is measured during the EDMR experiment has to be converted into a voltage before it can be detected. For this reason a SR570 preamplifier is used which converts and also amplifies the signal. It also comes with several band-pass, high-pass and low-pass filters which can be applied to the input current. Furthermore an input offset can be made which makes it possible to measure large currents in a sensitive range. The reference signal of the lock-in amplifier drives the modulation coils which are integrated in the cavity. The modulation frequency for all measurements in this thesis was set to 900 Hz. The measurement signal was modulated with this frequency and therefore has to pass through the preamplifier. The bandwidth of the different sensitivities is shown in table 3.1. For the EDMR measurement, the sensitivity range that was used to perform the measurements depends on the current of the signal and the bandwidth used. At a large current the system will go into overload. In order to measure larger currents at a higher sensitivity an input offset can be made. In general the highest possible sensitivity is chosen for the measurement. The limiting factor for the sensitivity range is the modulation frequency. As indicated in table 3.1 the range of 10^{-7} A/V has a bandwidth of 2 kHz while the 10^{-8} A/V range has a bandwidth of 0.2 kHz. This means that the measurement signal which is modulated with a frequency of 900 Hz cannot pass through the sensitivity range smaller than 10^{-7} A/V since the signal would be cut off.

Table 3.1: Specifications of the Stanford Research 570 current preamplifier in the low-noise mode.

Sensitivity A/V	Bandwidth /kHz	Noise /$\sqrt{\text{Hz}}$ pA
10^{-3}	1000.0	150.00
10^{-4}	500.0	60.00
10^{-5}	200.0	2.00
10^{-6}	20.0	0.60
10^{-7}	2.0	0.10
10^{-8}	0.2	0.06

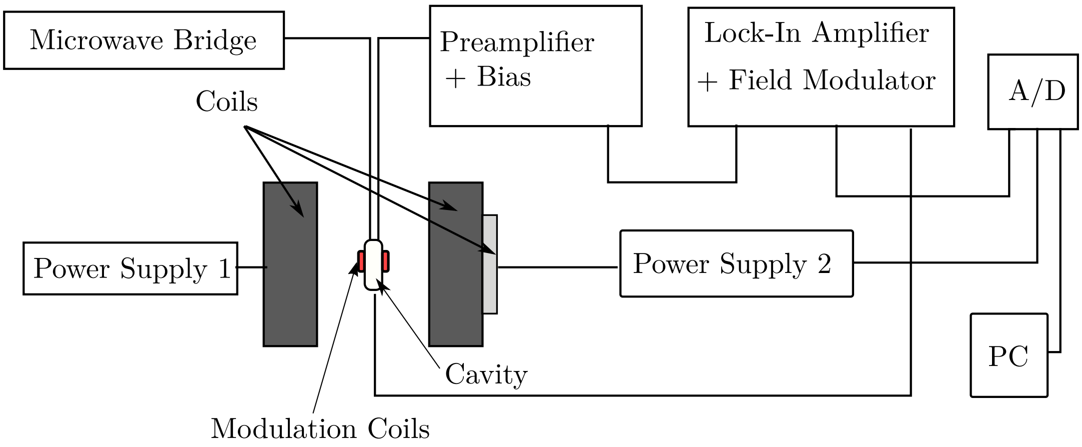

Figure 3.3: Schematic diagram of an EDMR setup. The sample is situated inside the microwave cavity and biased so that electrons and holes are injected into the device.

As mentioned above a low-pass filter can be applied to the input signal of the preamplifier. The measurement signal is modulated with the 900 Hz reference signal of the lock-in amplifier. In order to reduce the high frequency noise a low-pass filter with a cut-off frequency of 1 kHz and a slope of 12 dB is applied to the input signal. For spin dependent charge pumping measurements the low-pass filter is used for the integration of the AC signal. The integration of the signal yields the DC component of the charge pumping current which is used to calculate the D_{it} and perform the SDCP measurements. The preamplifier has a ±12 V output which is used to bias the MOSFET devices. The output voltage is connected to a home built metal box which consists out of several voltage dividers. This box is used for EDMR measurements with DC current. Furthermore it is also possible to bias the pin of the BNC connector at the input of the preamplifier remotely over a RS232 serial port which is used for the investigation of the diodes.

3.3 Sample Description

Before the devices under investigation were measured with the EDMR method, they were electrically characterized. Especially for the SiC diodes the electrical characterization gives a good insight into the biasing voltage that needs to be applied, to obtain a recombination current which can in principle be spin dependent.

3.3.1 SiC MOSFET

In this thesis two different MOSFETs were compared in the EDMR experiments. Both devices only differ in the post oxidation anneal (POA) which was conducted in an nitrous oxide (N_2O) or an oxygen (O_2) atmosphere under high temperature. Both devices were n-channel MOSFETs which were build on the Si-face of a 4H-SiC wafer. The body was p-doped with Al while the source and the drain were n-doped with N through an ion implantation process. Here the concentration of donors was $N_D \approx 10^{20}$ cm^{-3} while the concentration of acceptors was $N_A \approx 10^{17}$ cm^{-3}. The channel length of the device was 5.6 μm and the width was 100 μm. An oxide with a thickness of 80 nm was grown with a CVD process on both devices. The transfer characteristics of both devices were measured at room temperature and are shown in figure 3.4. Both devices were measured by connecting the source and the body contact. The drain contact was biased with different voltages. The drain current was measured, while the gate voltage was swept. The measurement was conducted for different drain voltages with a *Keithley 2636a* source meter. By comparing the transfer characteristics of both devices the influence of the POA can be seen. For positive gate voltages the N_2O device shows higher drain currents compared to the O_2 device. By using a negative drain voltage of $V_D \approx -2$ V the depletion region of the drain/body junction is getting narrower and the device turns on at lower gate voltages. Furthermore the source meter measures a current in the off-state at negative gate voltages, which is in the range of 10^{-10} A for both devices.

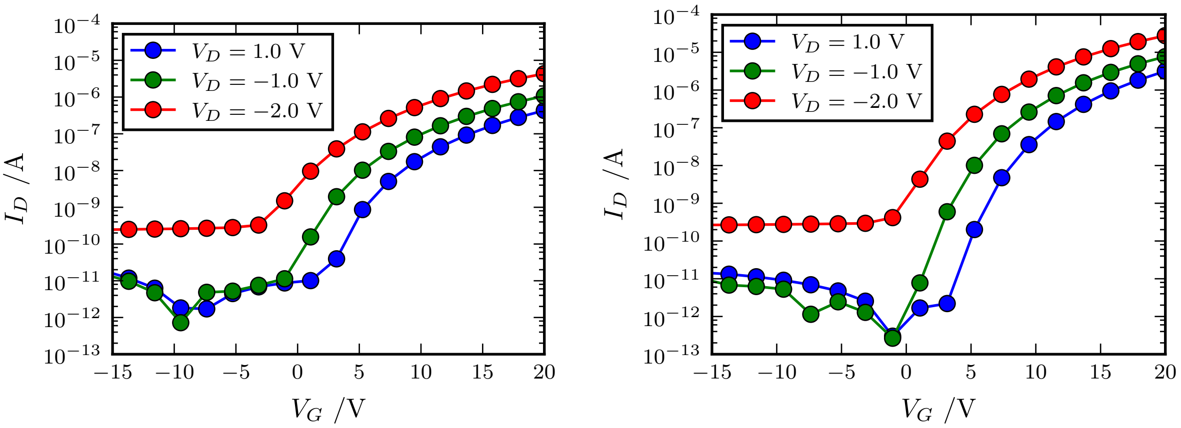

(a) O_2 Device (b) N_2O Device

Figure 3.4: Transfer characteristics of the two different MOSFET devices that were investigated with EDMR. Both devices were measured at different drain voltages while the body and the source contact were shorted and grounded.

For drain voltages above $V_D \approx -1$ V the leakage current is in the range of 10^{-11} A $- 10^{-13}$ A, which lies within the detection limit of the source meter.

3.3.2 SiC Diodes

The SiC diodes described in this section were implanted with nitrogen and showed a certain concentration of the carrier lifetime limiting defect $Z_{1/2}$, which was described in section 1.3. The three devices under investigation only differed in the annealing temperature. The different concentration of the defects were measured with deep level transient spectroscopy (DLTS) by F. Rasinger. In the following, the samples are referenced by the concentration of the $Z_{1/2}$ defect which was measured with DLTS. The annealing temperature of the sample with the low concentration was 1650°C while the one with the high concentration was 1800°C. The diode that showed a medium $Z_{1/2}$ concentration was annealed at 1725°C. Figure 3.5a shows the IV-characteristics of the various diodes that were investigated. In general all three devices showed a similar IV-characteristic. The DLTS measurements are shown in figure 3.5b. The DLTS signal at 330 K was assigned to the $Z_{1/2}$ defect. DLTS measurements of the $Z_{1/2}$ defect can be found in [24]. In this research the $Z_{1/2}$ peak was measured at a temperature of 300 K. The position of the peaks in DLTS depend on readout time. A shorter readout time shifts the peak towards a higher temperature. The recorded EDMR spectra can be found in section 3.6.

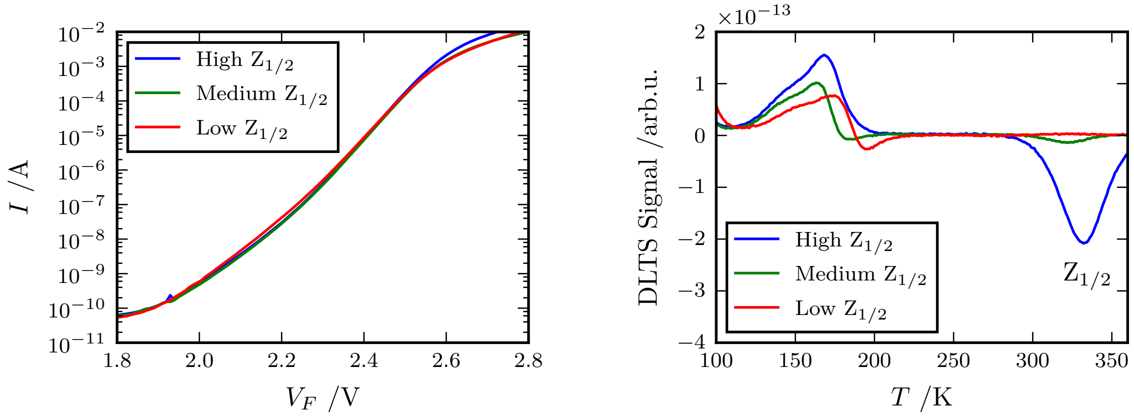

(a) IV-characteristics

(b) DLTS spectrum

Figure 3.5: (a) shows the IV-characteristics of the SiC diodes with a different $Z_{1/2}$ concentration. The different defect concentration in each sample does not influence the IV-characteristics. (b) shows the DLTS spectrum of the diodes. The signal at 330 K was assigned to the $Z_{1/2}$ defect.

3.4 Bipolar Amplification Effect (BAE)

The Bipolar Amplification Effect is a sensitive method to investigate defects at the semiconductor-oxide interface of MOSFET devices. The method was introduced by T. Aichinger *et al.* and yields EDMR spectra with a relative signal change $\Delta I/I$ that are more than one order of magnitude higher than the signals obtained with commonly used SDR techniques [5]. Interface traps are a limiting factor for all MOSFET devices. Figure 3.6 illustrates how an n-channel transistor is biased. The current is measured at the drain contact which is grounded, while the source body junction is forward biased. Here a negative voltage is applied to the source region while the body lies on the ground potential. Since the source/body junction is forward biased, the depletion region is small and minority carriers (electrons) are injected into the body region. The electrons diffuse into the p-region and a fraction of them will diffuse to the space charge region of the drain/body junction. The drain/body junction is not biased and the electrons will see a strong electric field and therefore get sucked into the drain region. If the diffusion length in the body is much smaller than the length of the channel between the source and the drain region, the minority electrons will recombine with the holes before they reach the drain region. The concentration of holes at the interface can be influenced by the gate voltage. The gate voltage is chosen so that there is a small current of several nA at the drain. In order to measure SDR at the interface of a MOSFET there has to be a minimum concentration of electrons, holes and defects. For this reason the device is not operated in the saturation regime where a n-channel would build up between the source and the drain region. For BAE measurements the device is operated in the cutoff regime.

In the commonly used SDR technique the MOSFET is biased as a gated diode, where the drain and the source are shorted and the current change is measured between the source-drain/body junction which is slightly forward biased. By operating the gate in accumulation there will be a high concentration of holes at the interface and only the defects in the depletion region at the source-drain/body junction will contribute to the SDR signal. If the gate is biased so that the interface traps lie within the depletion region they will contribute to the SDR signal [37]. The current between the junction in this technique is orders of magnitude larger than the drain current measured with the BAE, resulting in a lower relative signal for SDR.

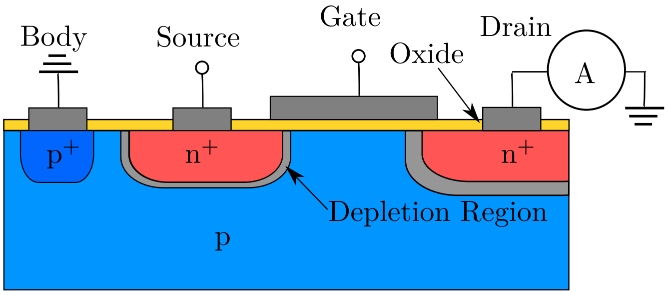

Figure 3.6: Schematic diagram of the BAE which shows the forward biased source/body junction and the unbiased drain/body junction. The gate is biased so that there is a small diffusion current between the source and the drain junction.

3.4.1 BAE Signals at Room Temperature

The two different devices described in section 3.3 were measured at room temperature at a fixed microwave frequency of 9.332 GHz. Both EDMR spectra are illustrated in figure 3.7. The source junction was biased with a voltage of −3.0 V while the gate voltage depended on the device. The gate voltage of the N_2O and O_2 device were −3.61 V and −5.75 V respectively. All BAE measurements were conducted at a microwave power of 0 dBm and a modulation amplitude of 1 G. Both EDMR signals were averaged over 200 sweeps in order to improve the SNR and show a strong peak with a g-value of 2.0038 for B||c. The defect was interpreted in terms of a carbon dangling bond at the interface [8].

The spectrum of the N_2O device (figure 3.7a) shows a broad line width which overlaps with the hyperfine structure that is ≈ ±6 G away from the resonance. The hyperfine structure of the O_2 device is nicely resolved compared to the N_2O device. Measurements at a lower microwave power yield the same hyperfine interaction for both devices which indicates that the dominant defect is same. The N_2O device shows additional peaks which are separated by ≈ 57 G. These peaks are not observed in the O_2 device which suggests that they are related to nitrogen. This doublet will be further investigated in section 3.4.3. Figure 3.7 shows that the relative EDMR signal of the O_2 device is higher than the one of the N_2O device. A reason for this might be that under the biasing conditions mentioned above more defects are measured in the O_2 device. G. Gruber investigated the relative signal of both devices under different biasing conditions [8]. It turned out that the N_2O device shows a higher maximum relative signal change than the O_2 device. This result contradicts the experimental results of figure 3.7 since the measurements were not conducted at the biasing conditions which yield the maximum relative EDMR signal. From charge pumping experiments it is known that the O_2 device has a higher density of interface traps than the N_2O device. Since the signal intensity of the BAE strongly depends on the biasing conditions, it is not possible to correlate the intensity of the EDMR spectrum with the density of interface traps that were obtained with charge pumping.

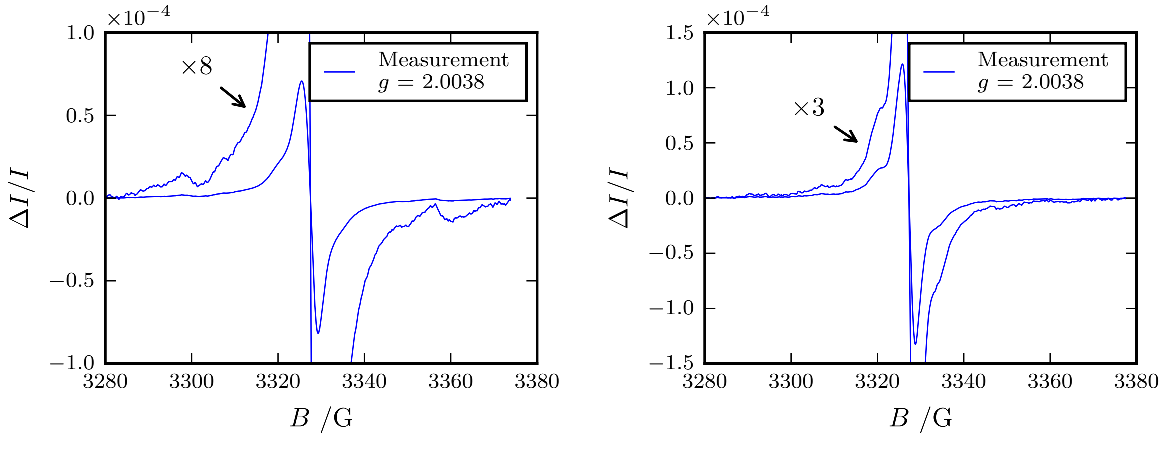

(a) N_2O device (b) O_2 device

Figure 3.7: Relative EDMR signals of both devices at room temperature. (a) shows the device with the N_2O and (b) the one with the O_2 post-oxidation anneal.

As shown in figure 3.7 the relative signal intensities strongly depend on the biasing conditions. It is currently not known if the relative BAE signal corresponds to the D_{it}. A better approach would be to compare the D_{it} with the relative EDMR signal of spin dependent charge pumping (SDCP) which is done later in this thesis.

3.4.2 Investigation of the Relative BAE Signal at Cryogenic Temperatures

The 57 G doublet of the N_2O device was found to vanish above room temperature [8]. For this reason it was of interest to investigate the doublet at lower temperatures. In order to perform low temperature measurements on the device it is important to investigate the behaviour of the BAE signal below room temperature. The relative signal $\Delta I/I$ obtained with the BAE method indicates how sensitive the measurement is and gives the fraction of the charge carriers that recombine under resonance. Therefore the signal's intensity is correlated to the amount of paramagnetic defects in the sample. Figure 3.8a shows the relative signal of the N_2O device at a temperature range from 30°C to −60°C. Every signal was measured under the same biasing conditions and a modulation amplitude of 1 G. The recorded spectra are single measurements since the signal to noise ratio (SNR) is sufficiently high. The source and the gate bias were set to −3.00 V and −3.61 V respectively. The figure shows that the relative signal increases with lower temperatures. In addition to the signal, also the noise level increases.

Figure 3.8b shows how the relative signal and the SNR depend on temperature. While the relative signal increases the SNR stays constant. The current I decreases with decreasing temperature. At temperatures lower than −60°C the current becomes too small for the sensitivity range of 10^{-7} A/V. Due to the limited bandwidth of the more sensitive ranges the range cannot be changed since the modulated signal cannot pass through the preamplifier without being cut off. The relative signal increases because the current I decreases faster than the absolute signal ΔI. In order to obtain BAE signals at temperatures below −60°C the biasing conditions have to be changed.

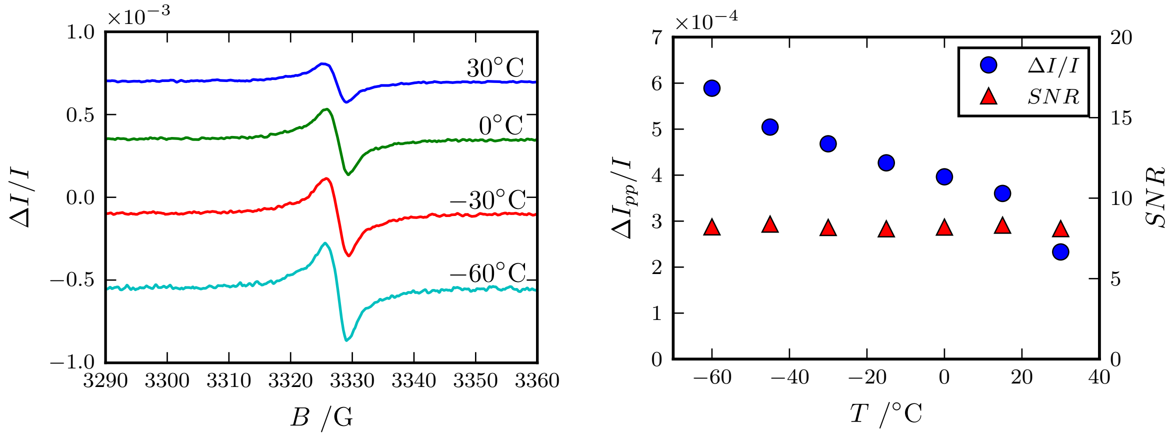

(a) Relative EDMR signal (b) Relative signal and SNR as a function of T

Figure 3.8: Relative EDMR signal of the N_2O device at different temperatures. (a) shows how the relative EDMR signals increase at lower temperatures. (b) shows how the relative signal change ($\Delta I_{pp}/I$) and the signal to noise ratio (SNR) depend on temperature.

The measurements at room temperature were conducted at a source voltage of −3.0 V. By lowering the temperature the drain current starts to decrease. This behaviour can be explained by describing the source-body and the drain-body junctions as pn-diodes. A pn-diode has a strong temperature dependence. The behaviour is dominated by the exponential factor $\exp(-E_g/k_BT)$. For this reason the source voltage was changed until the drain current was the same as at room temperature. Figure 3.9 shows how the relative signal for different temperatures and source voltages depend on the gate voltage. Until a gate voltage of $V_G = -4.0$ V the relative signal is approximately the same under all temperatures and source voltages. The deviation at gate voltages below −4.0 V is caused by the small drain currents, which were hard to read with the oscilloscope. For this reason low temperature measurements of the N_2O device with BAE were made at a gate voltage between −3.0 V and −4.0 V. The source voltage was adjusted in order to reach the same drain current as at room temperature.

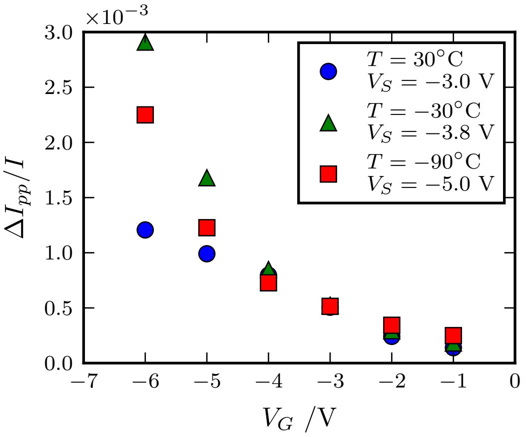

Figure 3.9: Relative signal under different biasing conditions and temperatures. The source voltage was adjusted so that the drain current at $V_G = -1.0$ V was the same as at room temperature.

3.4.3 Investigation of the 57 G Doublet at Cryogenic Temperatures

As mentioned before, the N_2O device shows an additional defect that has two peaks which are separated by 57 G. The spectrum is shown in figure 3.10. While the major defect can be seen in the center, the two side peaks are at 3300 G and 3357 G. The fact, that the doublet only appears in the device that experienced the N_2O post oxidation annealing indicates that the defect could be nitrogen related. The two peaks are centered at a different position than the major defect, which was identified to be a carbon dangling bond [8]. In case of a nitrogen related defect there should be a third line, which is situated in the center of the two visible side peaks, since nitrogen has a nuclear spin of $I = 1$. However, the problem with identifying an additional line in the center is the high signal intensity of the carbon dangling bond, which masks any other defect with a smaller intensity in this region. G. Gruber investigated the relative signal of the doublet with respect to the intensity of the carbon dangling bond [8]. The goal was to find measurement conditions where the intensity of the doublet would increase with respect to the intensity of the main defect in order to investigate the structure of the doublet. It was found that the doublet's intensity is independent of the microwave power and the gate voltage. However, the intensity of the doublet started to decrease with increasing temperature. In those experiments the temperature of the device was controlled with built-in polyheaters. The side peaks became continuously smaller with increasing temperature. At a temperature of 180°C, the two side peaks were barely visible. This behaviour raised the question how the doublet's intensity would change at lower temperatures. The lowest temperature where the doublet was measured was −90°C since signal averaging had to be performed and the measurement time was limited to the amount of liquid nitrogen in the dewar. Since the drain current decreases with decreasing temperature the source voltage had to be adjusted in order to measure a change in the current under the resonance condition. The source voltage at lower temperatures was changed until the drain current reached the value it had at room temperature. The measurements are illustrated in figure 3.10. All signals were averaged over 20 sweeps at a modulation amplitude of 3 G. The relative intensity of the doublet with respect to the intensity of the carbon dangling bond does not change at low temperature. Since at higher temperatures the intensity of the doublet decreases continuously it is unclear why they stay constant at lower temperatures.

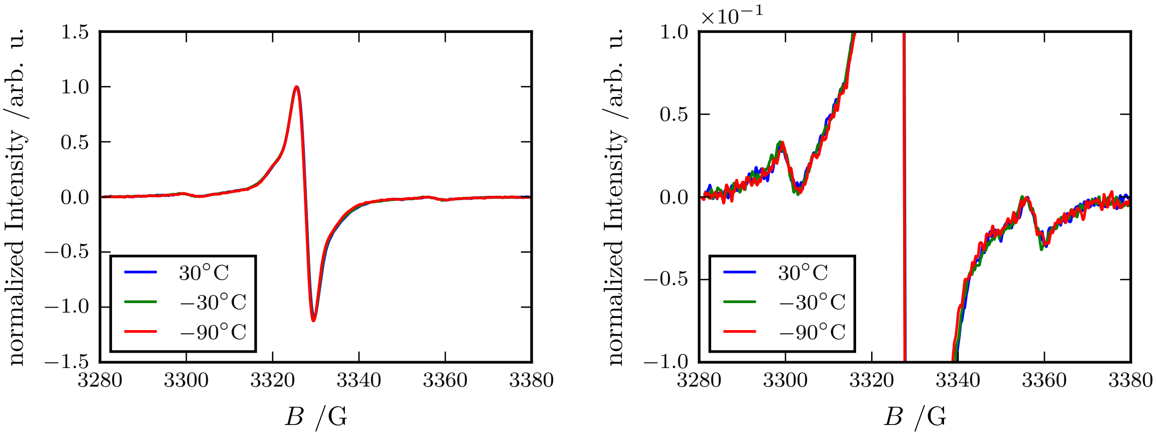

Figure 3.10: BAE measurement of the doublet that is observed in the N_2O device. The measurement was conducted at different temperatures and the signal was normalized in order to compare the intensity of the doublet.

3.5 Spin Dependent Charge Pumping (SDCP)

Spin dependent charge pumping is an EDMR technique that was first introduced by B. C. Bittel *et al.* [6, 38]. The method combines the interface sensitive charge pumping technique with EDMR. Charge pumping is the only method that allows for a quantitative electrical characterization of the interface of a MOSFET. Combined with EDMR it is a sensitive method for the investigation of paramagnetic defects at the semiconductor-oxide interface.

3.5.1 Electrical Characterization of MOSFETs with Charge Pumping

Before the spin dependent charge pumping technique is discussed this section will give a brief introduction into the electrical characterization of the semiconductor-oxide interface in a MOSFET with charge pumping. Most of what is written in this chapter can be found in more detail in [39].

The charge pumping method is based on the interaction between free carriers (electron, holes) and trap states at the interface of the semiconductor and the oxide. The source and the drain region are grounded while the gate is pulsed with a trapezoidal pulse between accumulation and inversion. An averaged current is measured at the substrate junction which is unbiased. The frequencies of the gate pulse are in the range of 10 kHz – 1 MHz. The biasing scheme is illustrated in figure 3.11. The following discussion will focus on n-channel devices which were investigated in this thesis. When the high phase of the pulse is applied to the gate the interface is in inversion and electrons are injected from the source and drain into the interface region of the MOSFET. Most of the electrons that are injected remain free in the conduction band, while a small fraction gets captured by the interface states. When the pulse switches from the high level to the low level the free electrons flow back into the source and drain regions, while the ones that are trapped remain at the interface. During the low phase the interface is in accumulation which allows the trapped electrons to recombine with the holes that are present at the interface. This means that the interface states store the minority charge carriers until the transition between inversion and accumulation happens. By using too steep rise and fall times between the high and low level of the pulse the free charge carriers cannot escape back into the source/drain region fast enough. This would add a parasitic component to the charge pumping current which should be avoided since the charge pumping current is used to determine the interface trap density. The number of trapped charges are scaled per unit area and to the probed energy window of the band gap that is accessible with charge pumping. This quantity is known as the density of interface states D_{it} and is given in the units of $\mathrm{eV} \cdot \mathrm{cm}^{-2}$:

$$D_{it} = \frac{I_{CP}^{max}}{A_{eff} f q \Delta E_{CP}} \tag{3.3}$$

where A_{eff} is the effective channel area, f is the frequency of the pulse, q is the elemental charge, ΔE_{CP} is the probed energy window of the band gap and I_{CP}^{max} is the maximum charge pumping current that is reached when the gate is biased fully in inversion and accumulation. The maximum charge pumping current is proportional to the frequency of the charge pumping pulse and the number of trapped charges per unit area N_{CP}:

$$I_{CP}^{max} = A_{eff} f q N_{CP} \tag{3.4}$$

The states at the interface can act as trapping centers or scattering centers and therefore influence the threshold voltage and the on-resistance of the device. Since charge pumping gives

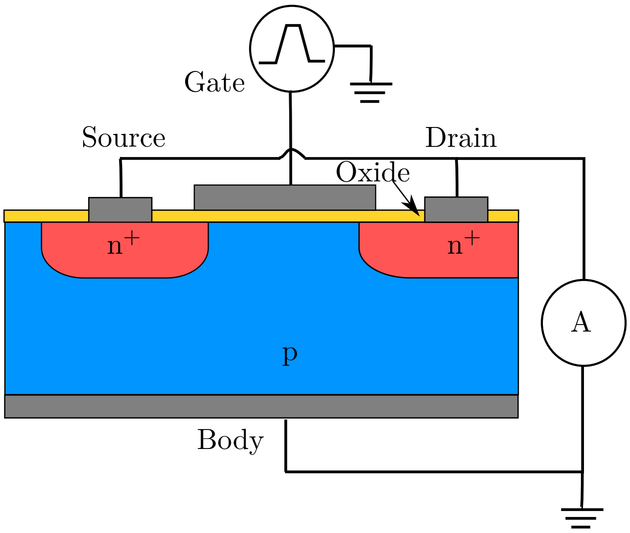

Figure 3.11: Biasing scheme of the charge pumping method. The source and the drain are shorted and the current is measured at the body junction. A trapezoidal pulse is applied on the gate.

a value for the amount of trapping centers at the interface it provides information about the quality of the semiconductor-oxide interface in a MOSFET. The method does not depend on variations in the channel doping, oxide thickness and threshold voltage which makes it ideal to compare devices with different oxide processing or defect passivation concepts. The trap states are energetically situated in the forbidden band gap of the semiconductor. The majority of the carriers are trapped in the interface states when the pulse goes from the high level to the low level or vice versa. However, states which are situated close to the valence or conduction band can have enough time to reemit the trapped carriers. These carriers do not contribute to the charge pumping signal. Since the switching between the high and the low level cannot be performed instantly, states near the band edges cannot be probed. For this reason only a certain energy window of the band gap is observable. The probed energy range depends on the switching time between the high and the low level of the pulse and the temperature. The transition probability between a trap in the forbidden band gap and the valence or conduction band is described by the transition time constant τ. It describes a 63 % chance that the transition between two levels will happen within the time interval τ. There are two types of transitions that can happen which are capture and emission processes. Capture and emission processes of electrons describe the transition between trap centers and the conduction band, while those of holes describe transitions between trap states and the valence band. An emission process requires energy and therefore describes the transition from a lower to a higher energy level. In a capture process the carrier loses energy through the transition.

The trapping and de-trapping in charge pumping occurs directly at the interface of the device. The filling of the traps happens during the high level of the pulse and the emptying through recombination occurs during the low phase. The time for filling and emptying the traps strongly depends on the high level V_{GH} and the low level V_{GL} of the pulse. In order to guarantee complete filling of the traps the high level of the pulse must exceed the charge pumping threshold V_{th}^{CP} and and the low level must lie beneath the charge pumping flat band voltage V_{fb}^{CP}. Only if this condition is satisfied the maximal charge pumping current I_{CP}^{max} is measured. The two quantities V_{th}^{CP} and V_{fb}^{CP} differ from the commonly used DC threshold and flat band voltages although they quantitatively lie in the same range. These two quantities are needed to calculate the probed energy window within the band gap. The upper emission boundary E_{en} and the lower emission boundary E_{ep} of the energy window is given by the following equations:

$$E_{en} = E_C - k_B T \ln \left(v_{thn} \sigma_n N_C \frac{\left(V_{th}^{CP} - V_{fb}^{CP} \right)}{\Delta V_G} t_f \right) \tag{3.5}$$

$$E_{ep} = E_V + k_B T \ln \left(v_{thp} \sigma_p N_V \frac{\left(V_{th}^{CP} - V_{fb}^{CP} \right)}{\Delta V_G} t_r \right) \tag{3.6}$$

where E_C and E_V are the band edges of the conduction and the valence band, T is the temperature, v_{thn} and v_{thp} are the thermal velocities for electrons and holes, σ_n and σ_p are the capture cross sections for electrons and holes and t_r and t_f are the rise and the fall time of the pulse. By subtracting the two equations above and using the relation for the intrinsic carrier concentration n_i showed in equation (1.15), the active energy window can be calculated out of the following equation:

$$\Delta E_{CP} = 2 k_B T \ln \left(\frac{\Delta V_G}{\sqrt{v_{thn} v_{thp}} n_i \sqrt{\sigma_n \sigma_p} \left(V_{th}^{CP} - V_{fb}^{CP} \right)} \sqrt{t_r t_f} \right) \tag{3.7}$$

In order to calculate the energy window, the charge pumping threshold and flat band voltage have to be determined experimentally. This is done with the constant base/high technique. The charge pumping threshold voltage is measured by keeping the low level constant and by sweeping the high level of the pulse and recording the charge pumping current. In case the high level exceeds the threshold voltage the charge pumping current will start to saturate. In order to determine the flat band voltage the high level is held constant, while the low level of the pulse is swept. The two characteristic voltages are extracted by numerically differentiating the curves. The threshold and flat band voltage are where the derivative shows a peak.

Since the quality of the interface of 4H-SiC MOSFETs is of high interest for industry, charge pumping is an ideal technique to electrically investigate the interface states in these devices. For more information on the investigation of SiC MOSFETs the reader is referred to [40].

3.5.2 SDCP Signals at Room Temperature

Spin dependent charge pumping combines the charge pumping technique described in section 3.5.1 with EDMR. Like BAE, the advantage in SDCP is that a background current does not have to be subtracted from the recombination current. Before SDCP experiments at lower temperatures were conducted, the signal's dependence on the microwave power, the frequency of the pulse and the rise and fall times of the pulse was investigated at room temperature in order to find the settings for an optimal signal to noise ratio (SNR). All measurements were conducted at a microwave frequency of 9.332 GHz, while the modulation frequency and the modulation amplitude were 900 Hz and 3 G respectively. In order to improve the SNR all measurements were averaged over 20 sweeps. Since both devices show the same dominating defect only the N_2O device was investigated in this section.

As a first approach the spectrum was obtained at different microwave powers. It is known from BAE that a higher microwave power causes a broadening of the spectrum's linewidth. The SDCP measurements in figure 3.12 show the spectrum at three different microwave powers. The measurements were obtained with a *Keithley 3390* arbitrary waveform generator at a pulse frequency of 100 kHz, an amplitude of ±10 V and a rise/fall time of 600 ns. In order to compare the quality of the different measurements, the signals were normalized. By changing the microwave power in the experiment, the photon density in the microwave resonator can be influenced. A higher photon density makes it more likely that a spin dependent recombination process will happen. However, the increase of the recombination processes will saturate at a certain microwave power. The results suggest that the defects at the interface are already saturated at a microwave power of −20 dBm. Furthermore the comparison of the different spectra in figure 3.12 suggests that the microwave power does not influence the SNR which contradicts previous investigations that were done with BAE [8].

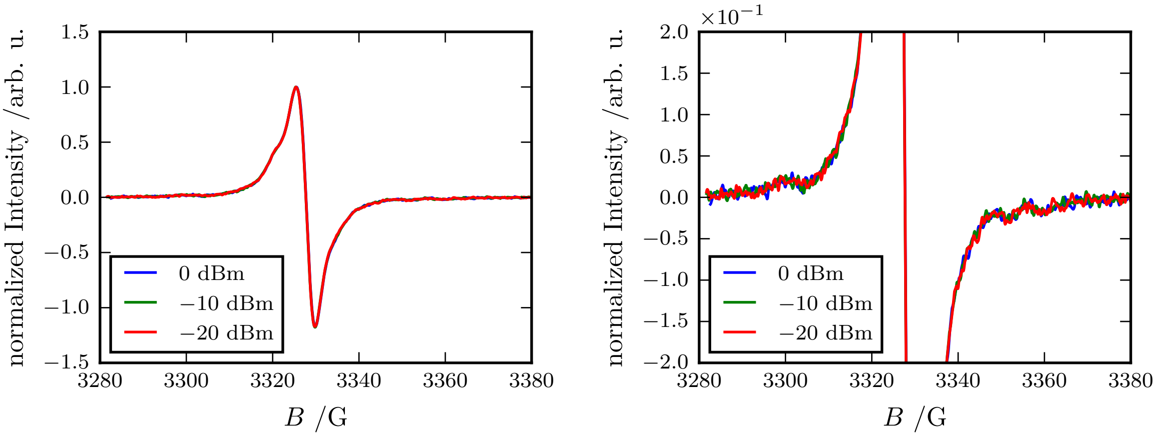

Figure 3.12: Normalized SDCP signal at room temperature for different microwave powers. Compared to BAE, the linewidth and the SNR of the SDCP signal does not depend on the microwave power.

The next parameter that can influence the SDCP signal was the frequency of the trapezoidal pulse that is applied on the gate. The maximum charge pumping current is proportional to the frequency of the applied pulse as shown in equation (3.4). The measurements are shown in figure 3.13 and were conducted at a pulse height of ±10 V, rise/fall times of 600 ns and a microwave power of 0 dBm. The enlarged spectrum clearly shows how the SNR improves with increasing frequency. The maximum frequency that was used was 200 kHz. At this frequency the doublet of the N_2O device is well resolved compared to the measurements at lower frequencies. At higher frequencies and longer signal averaging, device failure was an issue.

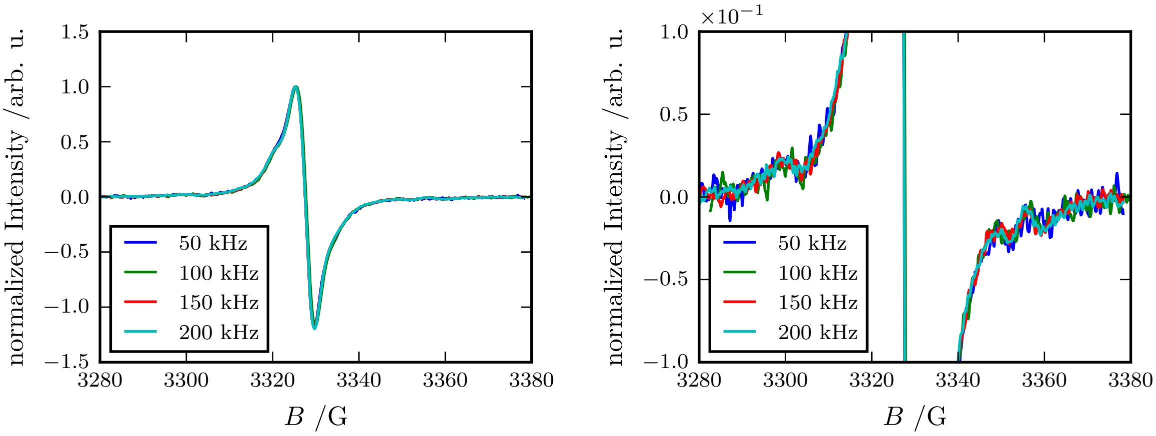

Figure 3.13: Normalized SDCP signals at room temperature for different pulse frequencies. The measurements show that at increasing frequencies the SNR improves.

Another parameter that can influence the quality of the signal is the rise and fall time of the pulse. As explained in section 3.5.1 the rise time has to be finite since during the transition from the high to the low level the free electrons need time to get back into the source/drain region. If this is not the case the charge pumping signal is distorted by a parasitic component [41]. As shown in equation (3.7) the rise and fall time influences the energy window that is probed during the charge pumping experiment. For this reason it can be expected that different rise and fall times influence the SDCP signal. The measurement was conducted at 100 kHz, ±10 V, 0 dBm and a constant fall time of 100 ns. By keeping the fall time of the pulse constant and by changing the rise time, the energy window is extended towards the conduction band. The measurements are illustrated in figure 3.14 and show that the noise increases with shorter rise times.

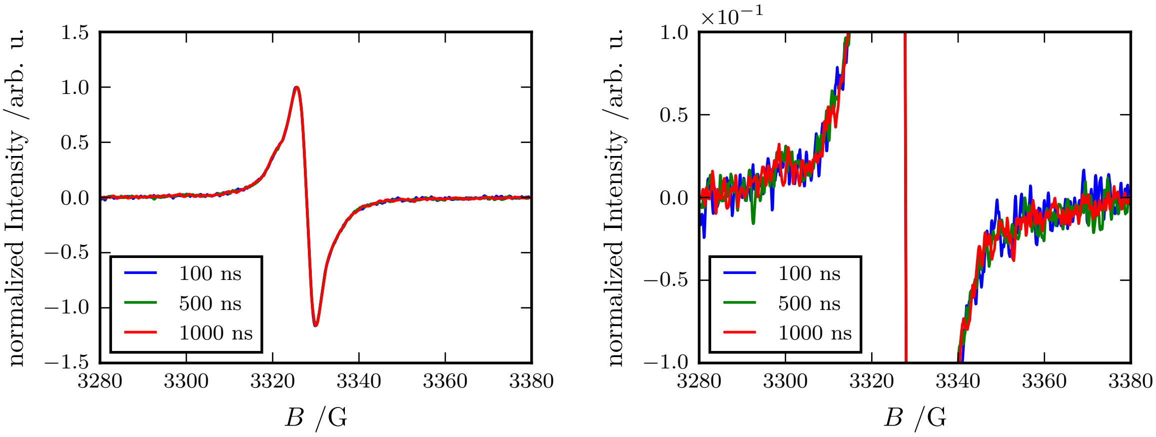

Figure 3.14: Normalized SDCP signals at room temperature for a constant fall time and different rise times. The measurements show that with increasing rise times the SNR improves.

3.5.3 Investigation of the Correlation between the relative SDCP Signal and the Density of Interface Traps

In order to investigate the relationship between the density of interface traps D_{it} and the spin dependent charge pumping (SDCP) signal, both devices were investigated with charge pumping (CP) and SDCP at different temperatures.

The density of interface states can be determined by investigating the devices with charge pumping. Therefore the active energy window ΔE_{CP} was calculated and the maximum charge pumping current I_{CP}^{max} was determined experimentally. The maximum charge pumping current is obtained when the interface is fully pulsed in inversion and accumulation. For this reason the high level of the pulse must exceed the charge pumping threshold voltage V_{th}^{CP} and the low level must lie beneath the charge pumping flat band voltage V_{fb}^{CP}. For both devices the pulse amplitude was set to a value of $V_G = \pm 25$ V. The energy window can be calculated with equation (3.7). Therefore V_{th}^{CP} and V_{fb}^{CP} has to be determined experimentally with the constant base/high level measurements, which are illustrated in figure 3.15 and 3.16 for both devices and for different temperatures. With decreasing temperature the probed energy window increases. In the two figures I_{CP}^{max} is the current at ±25 V. I_{CP}^{max} increases at low temperatures since there are more charge carriers trapped in the additional defects that can be seen with the increased energy window. As a result the D_{it} increases with decreasing temperature. The measurements, in figure 3.15 and 3.16, that start at -25 V and show a significant charge pumping current at $+25$ V are obtained with the constant base level technique and are used to extract V_{th}^{CP} for each device. The threshold voltage is extracted by numerically differentiating the signal and looking for the voltage at the peak of the derivative. For the N_2O device (figure 3.16) the V_{th}^{CP} increases with decreasing temperature while for the O_2 device (figure 3.15) the threshold increases at first and at a temperature of -120°C it decreases again. Furthermore at a temperature of -90°C degrees the maximum charge pumping current starts to saturate. The curves that start at $+25$ V and show the maximum current at -25 V are obtained with the constant high level technique. The charge pumping flat band voltage can be determined in analogy to the threshold voltage. With the charge pumping threshold and flat band voltage at each temperature it was possible to calculate the probed energy window with equation (3.7). In the experiment the difference between the high and the base level was $\Delta V_G = 50$ V while the rise and the fall time were both 600 ns. The capture cross section $\overline{\sigma}$ for electrons and holes has a value between 10^{-14} cm^2 $-$ 10^{-16} cm^2. Since the capture cross section was not known an intermediate value of 10^{-15} cm^2 was taken into account. The current at $+25$ V was extracted for each temperature as the maximum charge pumping current. Figure 3.17 shows the probed energy window for each temperature step and for both devices. With the experimentally determined values and equation (3.3) the density of interface states was calculated. The values for V_{th}^{CP}, V_{fb}^{CP}, ΔE_{CP}, I_{CP}^{max} and the D_{it} are listed in table 3.2 for both devices and for several temperatures. Figure 3.17 shows that the probed energy window is approximately the same for both devices since the V_{th}^{CP} and V_{fb}^{CP} do not differ too much. The O_2 and the N_2O device both have a D_{it} that is in the order of 10^{12} cm^{-2} eV. The O_2 device shows a slightly higher density of interface traps, which can be expected since it also has a higher maximum charge pumping current. The saturation of the maximum charge pumping current which starts at -90°C means that the amount of defects that are measured does not increase with further lowering the temperature. In general the passivation of defects in an O_2 atmosphere is poor which explains the high D_{it}. However, the annealing with N_2O shows only a rather small reduction of the D_{it}, which indicates that the N_2O annealing only had a small effect on defect passivation.

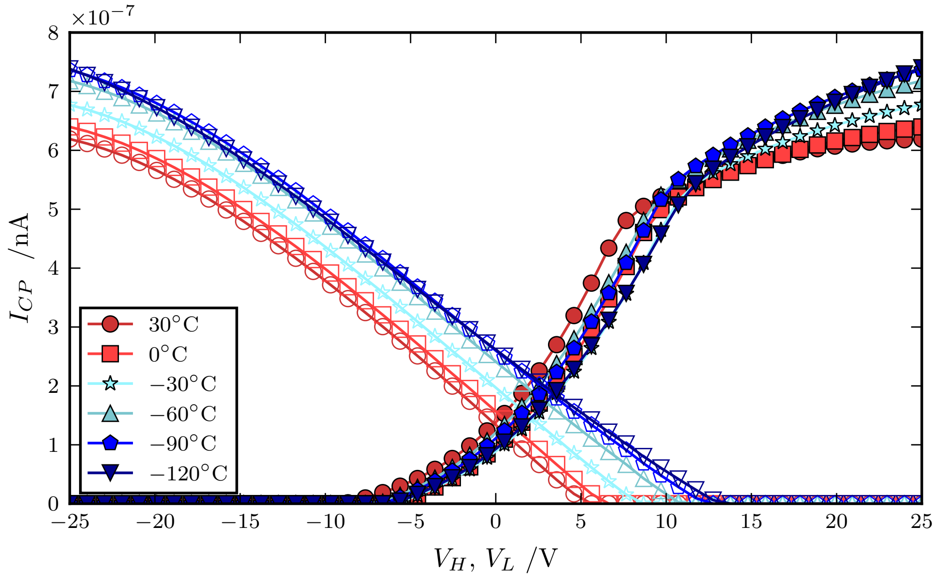

Figure 3.15: Charge pumping measurements with the constant base/high level technique of the O_2 device at different temperatures. The filled symbols indicate the constant base technique while the open symbols are the data points of the constant high level measurement.

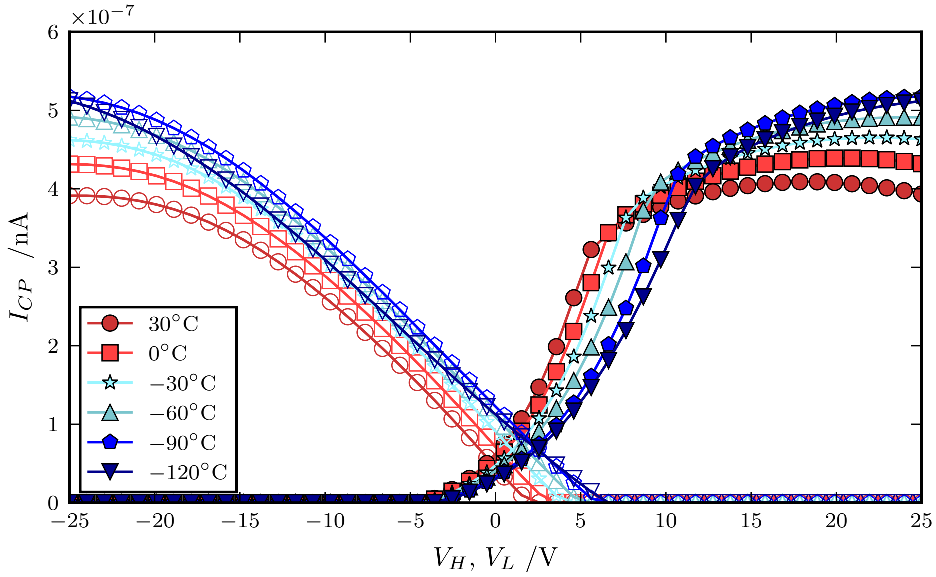

Figure 3.16: Charge pumping measurements with the constant base/high level technique of the N_2O device at different temperatures. The filled symbols indicate the constant base technique while the open symbols are the data points of the constant high level measurement.

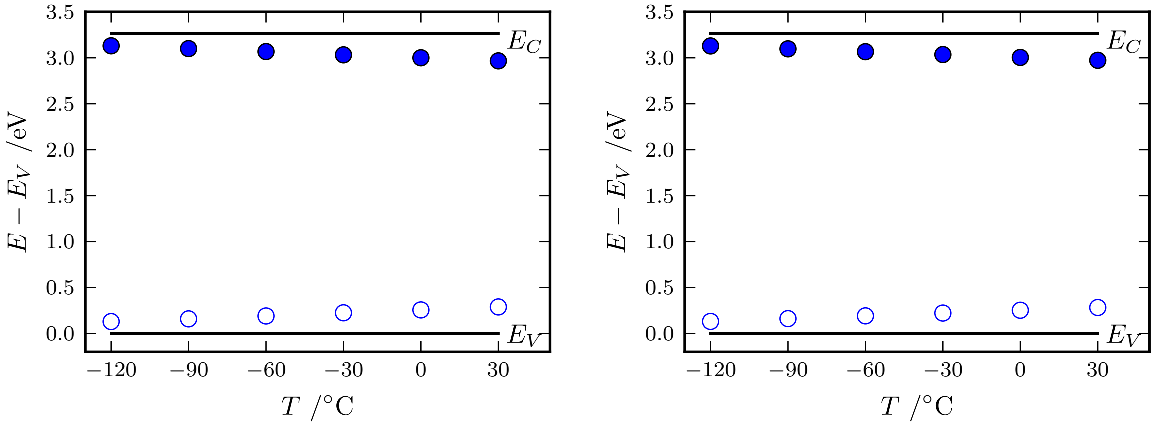

(a) O_2 Device

(b) N_2O Device

Figure 3.17: (a) and (b) show the energy window for the O2 and N2O device at different temperatures. With decreasing temperature a bigger energy range of the band gap is accessible with charge pumping.

A state of the art annealing in SiC technology is done with NO, however the process passivates most of the paramagnetic defects in the device which makes an SDCP measurement rather difficult. Long signal averaging is needed which is not possible at low temperatures due to the limited amount of liquid nitrogen that is available for cooling. Both devices were measured with SDCP at a pulse of 100 kHz, an amplitude of ±25 V and rise/fall times of 600 ns. These are the same conditions under which the constant high and base level measurements were performed. The signal intensity of the SDCP measurements depends on the amount of defects that are measured. By performing CP and SDCP measurements under the same conditions the signal intensity correlates with the amount of spin-dependent interface traps.

Table 3.2: Important parameters that were extracted out of the constant base and high level measurements at each temperature step. The active energy window and the density of interface traps were calculated out of the extracted parameters.

Device	T /°C	V_{th}^{CP} /V	V_{fb}^{CP} /V	ΔE_{CP} /eV	I_{CP}^{max} /nA	D_{it} /10^{12} cm^{-2} eV
O2	30	5.44	-8.28	2.64	619	2.43
	0	7.86	-7.38	2.71	639	2.44
	-30	8.77	-7.52	2.78	677	2.52
	-60	7.70	-7.28	2.86	718	2.60
	-90	7.80	-7.08	2.93	737	2.60
	-120	7.50	-7.00	2.99	740	2.56
N2O	30	3.68	-6.66	2.66	393	1.53
	0	4.7	-6.99	2.73	432	1.64
	-30	5.78	-7.23	2.79	463	1.72
	-60	6.93	-7.46	2.86	491	1.78
	-90	8.52	-7.61	2.92	516	1.83
	-120	9.28	-7.74	2.99	511	1.77

The recorded SDCP spectrum for both devices is illustrated in figure 3.18. The figure compares the SDCP signal ΔI at room temperature and -120°C. Since in charge pumping lower temperatures probe a larger part of the band gap and the D_{it} increases towards the band edges, it is expected that a higher amount of defects can be measured with SDCP at lower temperatures. This is in good agreement with the rising SDCP signal at low temperatures that can be seen in figure 3.18. However it seems odd that the signal of the N_2O device rises faster than the one of the O_2 device. This contradicts the conclusion that the higher density of interface states can be observed in the O_2 device. Note that with any EDMR technique only paramagnetic defects are accessible during the measurement. In a CP experiment also defects that are not accessible to EDMR are measured. The results indicate that no reliable statement can be made about the fraction of the D_{it} that is paramagnetic. The results suggest that a fraction of the D_{it} that is measured with CP seems to be not accessible with SDCP.

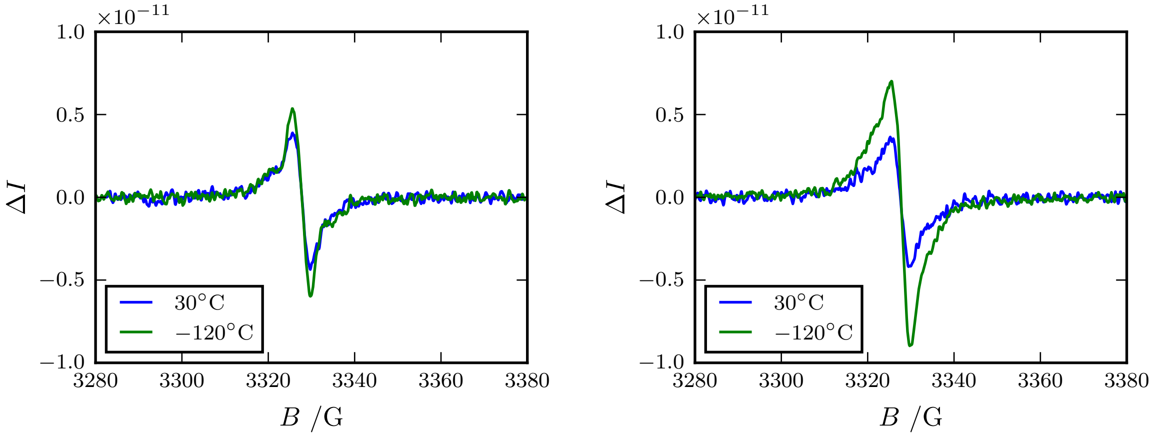

(a) O_2 Device

(b) N_2O Device

Figure 3.18: SDCP signal for both devices and at different temperatures. The N_2O device shows a higher signal at lower temperatures compared to the O_2 device.

Since the charge pumping current rises with decreasing temperature, the relative SDCP signal $\Delta I/I$ was of certain interest. Figure 3.19 shows the relative signals for both devices at room temperature and at -120°C. The relative signal of the N_2O device increases with decreasing temperature (figure 3.19b), while the relative signal of the O_2 device remains constant (figure 3.19a). This behaviour can be explained by comparing the current change ΔI with the charge pumping current I at both temperatures. The signal intensity scales linearly with the charge pumping current which explains why the relative signal stays constant from room temperature to -120°C. The ratio of ΔI and I quantifies what fraction of the current recombines over paramagnetic defect centers. Therefore the signals in figure 3.19b suggest that at low temperatures a bigger part of the charge pumping current recombines over paramagnetic defect centers in the N_2O device. As mentioned before, at low temperatures trapping states near the band edges are accessible with charge pumping. By comparing the relative signal of both devices at -120°C the results could imply that there are more paramagnetic defect centers near the band edges in the N_2O device. The recombination current and the relative current change at different temperatures were listed in table 3.3.

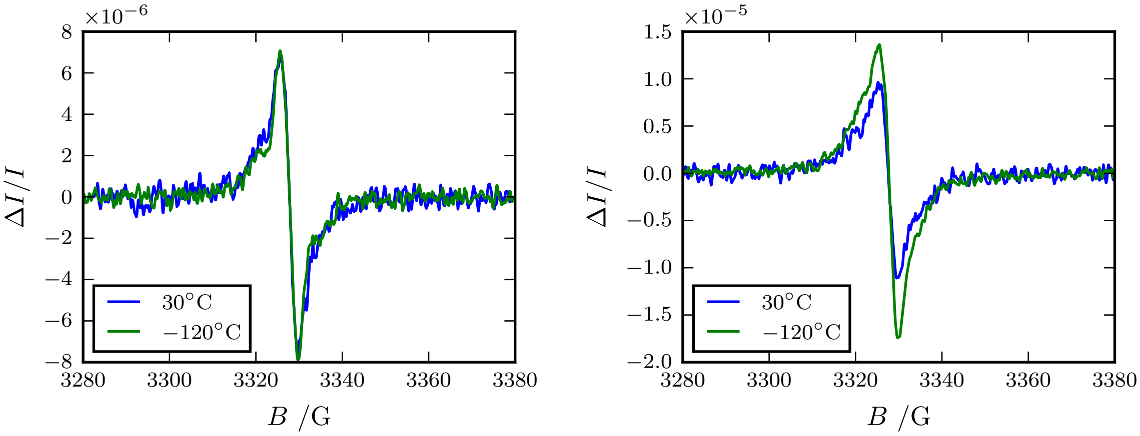

(a) O_2 Device

(b) N_2O Device

Figure 3.19: Relative SDCP signal for both devices and at different temperatures. The N_2O device shows a higher signal at lower temperatures compared to the O_2 device.

Table 3.3: Comparison of the recombination current and the relative current change of both devices and at different temperatures.

Device	T /°C	ΔI_{CP} /10^{-14}A	I_{CP} /nA	$\Delta I_{CP}/I_{CP}$ /10^{-8}
O_2	30	0.94	619	1.68
	-120	1.04	740	1.27
N_2O	30	1.25	393	3.18
	-120	2.16	511	4.23

3.5.4 Comparison of the SDCP and the BAE Signals

Both devices that were investigated in this thesis were measured with the bipolar amplification effect (BAE) and spin dependent charge pumping (SDCP). BAE and SDCP are two different EDMR techniques, however with both it is possible to measure the same defect [21]. The measurement of both devices is shown in figure 3.20. The signal was normalized in order to compare the hyperfine structure. All measurements were averaged over 200 sweeps in order to improve the signal to noise ratio (SNR). The SDCP measurements were conducted with a pulse of 600 ns rise/fall time and an amplitude of ±10 V at room temperature. The N_2O and the O_2 devices were measured with a pulse frequency of 200 kHz and 120 kHz respectively. For the BAE measurements, the source voltage was set to -3.0 V, while the gate voltage was set to -3.6 V for the N_2O device and -5.8 V for the O_2 device. All spectra were recorded at a microwave power of 0 dBm.

The hyperfine interaction of the O_2 device in figure 3.20a shows a shoulder in both measurements. However the linewidth of the BAE method seems to be a bit smaller than the one of the SDCP measurement although both were measured at the same microwave power. The noise of the SDCP measurement is also slightly higher than the one of the BAE measurement. The 57 G doublet of the N_2O device can be seen in figure 3.20b at a magnetic field of 3300 G and 3357 G.

It was measured with both methods, however it is better resolved with BAE. Furthermore the SDCP signal is also slightly broader compared to the BAE signal.

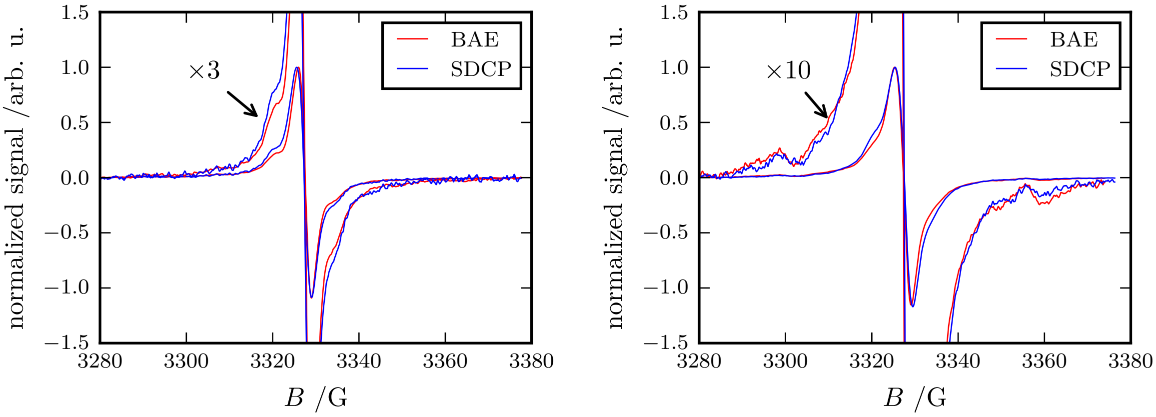

(a) O_2 Device

(b) N_2O Device

Figure 3.20: Comparison of the EDMR spectra of the BAE and the SDCP measurement for both devices. The signal was normalized in order to compare the signal shape and the hyperfine structure. Both measurements yield the same defect.

By comparing the relative signal of both methods in figure 3.21 it can be seen that the spectrum obtained with BAE shows a relative signal that is orders of magnitude higher than the one of the SDCP spectrum. This shows that BAE is a more sensitive method compared to SDCP. However, the advantage of SDCP is that the energy window that is probed during the measurement can be calculated by determining V_{th}^{CP} and V_{fb}^{CP} experimentally in a charge pumping experiment.

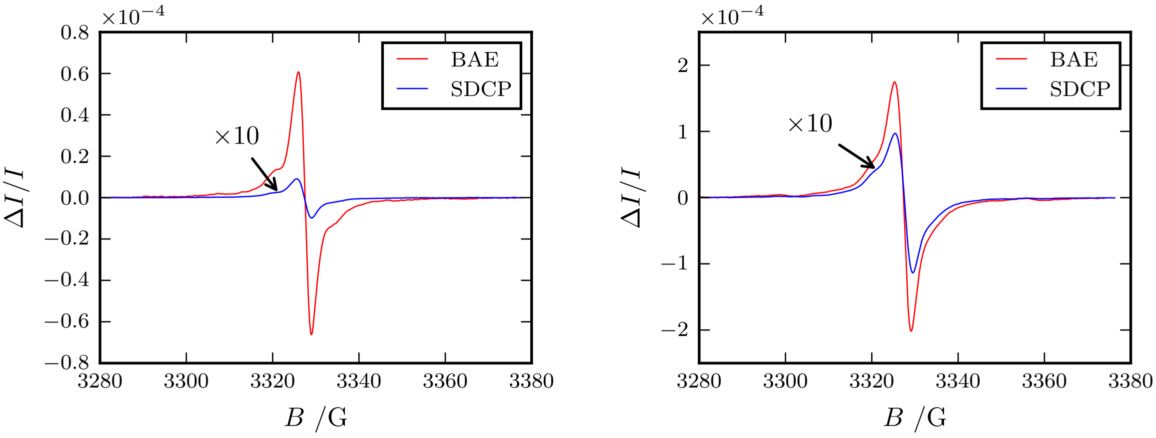

(a) O_2 Device

(b) N_2O Device

Figure 3.21: Comparison of the relative Signal of BAE and SDCP. BAE shows an order of magnitude higher relative signal than the one obtained with SDCP.

3.6 Spin Dependent Recombination (SDR) Measurements of SiC Diodes

The samples investigated in this section were SiC diodes that were implanted with nitrogen and annealed at different temperatures. An investigation with deep level transient spectroscopy (DLTS) showed that the three samples had a different concentration of the carrier lifetime limiting defect $Z_{1/2}$. The DLTS spectrum was shown in figure 3.5b. The defect was identified as a carbon vacancy by K. Kawahara *et. al* [24] and is described in section 1.3. In their research they irradiated n-type 4H-SiC with electrons of an energy of 250 keV and therefore obtained different concentrations of $Z_{1/2}$. They performed measurements with electron paramagnetic resonance (EPR) and DLTS. However, with EPR only paramagnetic defects can be observed. In equilibrium the carbon vacancy exists in the charge states V_C^{-2} and V_C^0 which are not EPR active [24]. In order to perform EPR measurements of the carbon vacancies which are in a non-paramagnetic charge state, the sample was illuminated with light in order to activate the V_C^- centers. Under illumination the EPR spectrum shows two dominating peaks due to the different energies of a V_C^- center at a cubic $V_C^-(k)$ or hexagonal $V_C^-(h)$ site. The EPR signal of the cubic and hexagonal site was strongly dependent on the photon energy [42]. The g-values for $B \parallel c$ were 2.0048 and 2.0040 [24]. The EPR measurement was conducted at a temperature of 100 K.

So far a measurement of $Z_{1/2}$ with EDMR was not conducted according to literature. The IV-characteristics of the investigated diodes can be found in section 3.3.2. The samples are referred to in terms of the intensity of the DLTS signal. The intensity of the DLTS signal is proportional to the concentration of the investigated defect. The EDMR spectra are shown in figure 3.22. Since the samples showed a weak EDMR signal the measurements were recorded at a modulation amplitude of 6 G and were averaged over 200 sweeps. In general all devices seem to show an isotropic g-value, which was measured at $B \parallel c$ and $B \perp c$. The sample with the low $Z_{1/2}$ concentration in figure 3.22a shows a g-value of 2.0044. The spectrum might indicate that two defects overlap and they cannot be resolved due to the high modulation amplitude. The g-value is similar to the one of the carbon vacancy measured in [24], however it shows an isotropic behaviour. For this reason it can be ruled out that the spectrum shows the carbon vacancy and therefore the $Z_{1/2}$ defect. The spectrum of the diodes that showed a medium and high $Z_{1/2}$ concentration also yield an isotropic g-value of 2.0032 and 2.0033. The spectra are shown in figure 3.22b and 3.22c. The g-values are in good agreement to the one of the silicon vacancy which is $g \approx 2.0034$ [20]. The relative signal of the EDMR signal does not correspond to the concentrations of the $Z_{1/2}$ defect measured with DLTS. This indicates that the defects measured are not the carbon vacancy. A reasonable explanation would be that the carbon vacancy measured with DLTS is in a charge state that is not paramagnetic, which is described in [24]. Furthermore the defect measured with EDMR is isotropic, while the g-value of the carbon vacancy shows an angular dependence. An identification of the defects measured with EDMR turns out to be very difficult since the signal is too weak to resolve the hyperfine structure. The modulation amplitude is too high to resolve small features of the spectrum.

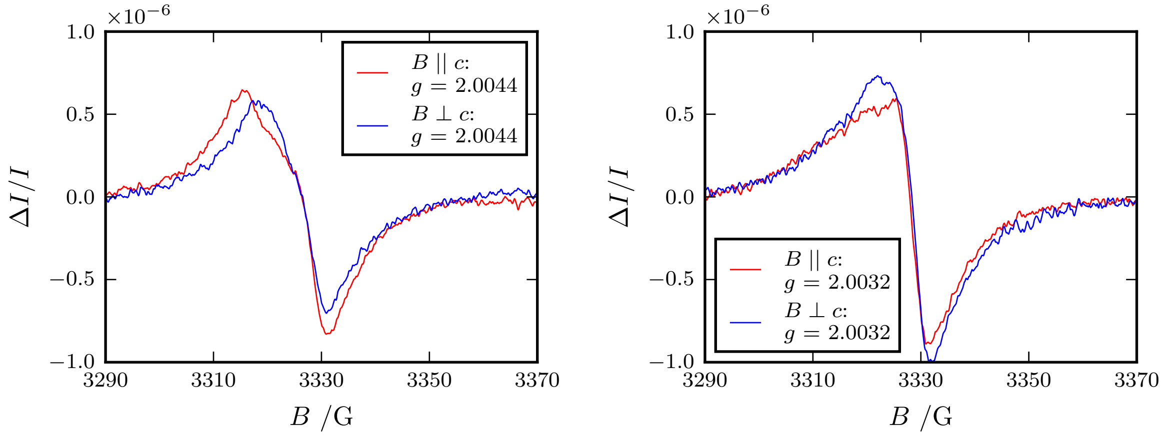

(a) Low $Z_{1/2}$ concentration (b) Medium $Z_{1/2}$ concentration

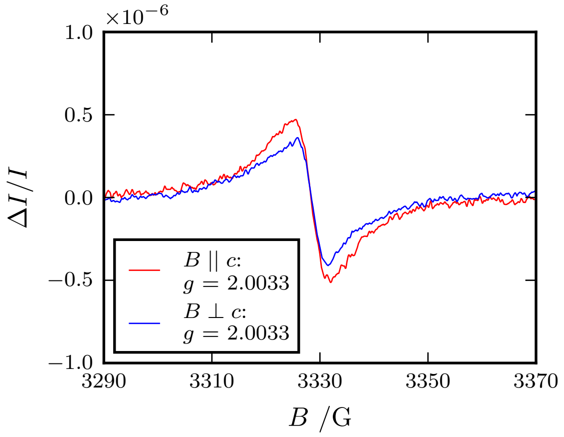

(c) High $Z_{1/2}$ concentration

Figure 3.22: EDMR spectra of the SiC diodes, which showed a different concentration of the $Z_{1/2}$ defect in a DLTS experiment. All spectra show isotropic g-values. The sample with the low $Z_{1/2}$ concentration shows a different g-value compared to the diodes with the higher $Z_{1/2}$ concentration.

Chapter 4

Summary and Conclusion

In this work SiC MOSFETs and nitrogen implanted SiC diodes were investigated with different EDMR techniques. The MOSFETs were measured at cryogenic temperatures, while the measurements of the diodes were conducted at room temperature. The EDMR measurements were performed in an X-band microwave cavity.

Two different n-channel SiC MOSFETs were investigated with the bipolar amplification effect (BAE) and spin dependent charge pumping (SDCP). The devices differed in the annealing gas that was used for the passivation of interface traps at the semiconductor-oxide interface. For the investigated devices, O_2 and N_2O were used as annealing gases. Investigations with the BAE method already showed that both devices show the same dominating paramagnetic defect in the EDMR spectrum, which was identified as a carbon dangling bond [8]. Furthermore the N_2O device showed two additional peaks with a 57 G splitting. It was shown that these peaks start to vanish at temperatures above room temperatures [8]. In this work the side peaks in the N_2O device were measured with EDMR at several temperatures below room temperature. It was shown that cryogenic temperatures do not affect the intensity of the side peaks. In general the resolution of the BAE signal could not be improved at cryogenic temperatures. Although the relative change in the recombination current increased at low temperatures the signal to noise ratio (SNR) remained constant.

Another approach to gain more information about the defect at cryogenic temperatures was SDCP. The method combines charge pumping (CP) with EDMR. CP can be used to calculate the density of interface traps D_{it} and the probed energy window ΔE_{CP} within the semiconductor band gap. It is known that the D_{it} increases towards the band edges and cryogenic temperatures make it possible to probe a larger area of the band gap [39]. The CP experiments showed that the O_2 device has a higher D_{it} than the N_2O device. The CP method makes it possible to measure two differently processed devices under the same measurement conditions and to compare them. In the SDCP experiments both devices showed a similar signal intensity, while at low temperatures the signal of the N_2O device was larger. This contradicts to the higher D_{it} in the O_2 device. Since for both devices the same energy window was probed the reason for the larger SDCP signal in the N_2O device might be a larger amount of paramagnetic defects, which are energetically situated near the band edges. The amount of defects at the interface is proportional to the current measured in a CP experiment. For this reason the ratio between the recombination current and the charge pumping current gives evidence of the amount of defects that contribute to the EDMR signal. The relative signal change $\Delta I/I$ is in the order of 10^{-8} which indicates that a lot of defects contributing to the D_{it} in the CP experiment are not paramagnetic and therefore not accessible to EDMR. By comparing the BAE and the SDCP measurements it was shown that the BAE spectrum shows a better SNR and a higher relative change in the recombination current. Both methods yielded the same g-value and the same hyperfine (HF) structure. The 57 G doublet that was observed in the N_2O device was resolved with both methods.

Nitrogen implanted diodes with different concentrations of the carrier lifetime limiting defect $Z_{1/2}$ were investigated with EDMR at room temperature. Three wafers were implanted with nitrogen and annealed at different temperatures. The wafers were investigated with deep level transient spectroscopy (DLTS). The DLTS spectra of the diodes showed that they have a different concentration of the $Z_{1/2}$ defect. In literature the $Z_{1/2}$ defect was investigated in irradiated SiC crystals with DLTS and electron paramagnetic resonance (EPR) and was identified as a carbon vacancy [24]. However, there is currently no research that compares the DLTS spectrum to a EDMR spectrum in an industrial processed device. For this reason the samples were investigated with EDMR. All diodes gave a weak EDMR signal although they were measured with a modulation amplitude of 6 G and they were averaged over 200 sweeps. A significant difference in the intensity of the EDMR signal was not observed for the various samples. All diodes showed an isotropic g-value. The HF structure could not be resolved since the SNR was too small. For this reason it is not possible to identify the defect. The g-value and its isotropic nature suggest that it could be a silicon vacancy [20]. Due to the fact that the three differently processed diodes show a different concentration of the $Z_{1/2}$ defect in DLTS, but show a similar signal intensity in the EDMR experiment, the defect measured with EDMR is most likely not $Z_{1/2}$. This indicates that the defect is in a non paramagnetic charge states. For this reason $Z_{1/2}$ cannot be probed with EDMR.

In order to receive spectra with a better resolution future experiments could be performed at microwave frequencies in the W-band. It was shown in literature that W-band experiments show a better resolution and a relative signal change that is two orders of magnitude higher than in X-band measurements [43].

Bibliography

[1] Adrian R Powell and Larry B Rowland. SiC materials-progress, status, and potential roadblocks. *Proceedings of the IEEE*, 90(6):942–955, 2002.

[2] Philip G Neudeck, Robert S Okojie, and Liang-Yu Chen. High-temperature electronics-a role for wide bandgap semiconductors? *Proceedings of the IEEE*, 90(6):1065–1076, 2002.

[3] D.M. Fleetwood and R.D. Schrimpf. *Defects in Microelectronic Materials and Devices.* CRC Press, 2008.

[4] Martin Stutzmann, Martin S Brandt, and Martin W Bayerl. Spin-dependent processes in amorphous and microcrystalline silicon: a survey. *Journal of non-crystalline solids*, 266:1–22, 2000.

[5] Thomas Aichinger and Patrick M Lenahan. Giant amplification of spin dependent recombination at heterojunctions through a gate controlled bipolar effect. *Applied Physics Letters*, 101(8):083504, 2012.

[6] BC Bittel, PM Lenahan, JT Ryan, J Fronheiser, and AJ Lelis. Spin dependent charge pumping in SiC metal-oxide-semiconductor field-effect-transistors. *Applied Physics Letters*, 99(8):083504, 2011.

[7] Hui Deng, Katsuyoshi Endo, and Kazuya Yamamura. Competition between surface modification and abrasive polishing: a method of controlling the surface atomic structure of 4H-SiC (0001). *Scientific reports*, 5, 2015.

[8] Gernot Gruber. *Performance and Reliability Limiting Point Defects in SiC Power Devices.* PhD thesis, Technical University of Graz, 2016.

[9] F. Ren and J.C. Zolper. *Wide Energy Bandgap Electronic Devices.* World Scientific, 2003.

[10] Tsunenobu Kimoto, Akira Itoh, Hiroyuki Matsunami, and Tetsuyuki Okano. Step bunching mechanism in chemical vapor deposition of 6H–and 4H–SiC {0001}. *Journal of Applied Physics*, 81(8):3494–3500, 1997.

[11] Mikael Syväjärvi, Rositsa Yakimova, and Erik Janzén. Step-bunching in SiC epitaxy: anisotropy and influence of growth temperature. *Journal of crystal growth*, 236(1):297–304, 2002.

[12] J. Fan and P.K.H. Chu. *Silicon Carbide Nanostructures: Fabrication, Structure, and Properties.* Engineering Materials and Processes. Springer International Publishing, 2014.

[13] VV Afanasev, M Bassler, G Pensl, and M Schulz. Intrinsic SiC/SiO2 interface states. *physica status solidi (a)*, 162(1):321–337, 1997.

[14] Y Song, S Dhar, LC Feldman, G Chung, and JR Williams. Modified deal grove model for the thermal oxidation of silicon carbide. *Journal of applied physics*, 95(9):4953–4957, 2004.

[15] Pietro Mandracci, Sergio Ferrero, Carlo Ricciardi, Luciano Scaltrito, G Richieri, and C Sgorlon. Low temperature growth of SiO2 on SiC by plasma enhanced chemical vapor deposition for power device applications. *Thin Solid Films*, 427(1):142–146, 2003.

[16] A.C. Jones and M.L. Hitchman. *Chemical Vapour Deposition: Precursors, Processes and Applications*. Royal Society of Chemistry, 2009.

[17] Tsunenobu Kimoto and James A Cooper. *Fundamentals of Silicon Carbide Technology: Growth, Characterization, Devices and Applications*. John Wiley & Sons, 2014.

[18] P. Friedrichs, T. Kimoto, L. Ley, and G. Pensl. *Silicon Carbide: Volume 1: Growth, Defects, and Novel Applications*. Wiley, 2011.

[19] J Isoya, T Umeda, N Mizuochi, Nguyen Tien Son, Erik Janzén, and T Ohshima. EPR identification of intrinsic defects in SiC. *physica status solidi (b)*, 245(7):1298–1314, 2008.

[20] T Wimbauer, BK Meyer, A Hofstaetter, A Scharmann, and H Overhof. Negatively charged Si vacancy in 4H SiC: A comparison between theory and experiment. *Physical Review B*, 56(12):7384, 1997.

[21] CJ Cochrane, PM Lenahan, and AJ Lelis. The effect of nitric oxide anneals on silicon vacancies at and very near the interface of 4H SiC metal oxide semiconducting field effect transistors using electrically detected magnetic resonance. *Applied Physics Letters*, 102(19):193507, 2013.

[22] NT Son, PN Hai, and Erik Janzén. Carbon vacancy-related defect in 4H and 6H SiC. *Physical Review B*, 63(20):201201, 2001.

[23] T Umeda, Y Ishitsuka, J Isoya, NT Son, Erik Janzén, N Morishita, T Ohshima, H Itoh, and A Gali. EPR and theoretical studies of negatively charged carbon vacancy in 4H-SiC. *Physical review B*, 71(19):193202, 2005.

[24] Koutarou Kawahara, Xuan Thang Trinh, Nguyen Tien Son, Erik Janzén, Jun Suda, and Tsunenobu Kimoto. Quantitative comparison between Z1/2 center and carbon vacancy in 4H-SiC. *Journal of Applied Physics*, 115(14):143705, 2014.

[25] Jean-Louis Cantin, HJ Von Bardeleben, Y Shishkin, Y Ke, RP Devaty, and WJ Choyke. Identification of the carbon dangling bond center at the 4H-SiC/SiO2 interface by an EPR study in oxidized porous SiC. *Physical review letters*, 92(1):015502, 2004.

[26] S.M. Sze and K.K. Ng. *Physics of Semiconductor Devices*. Wiley, 2006.

[27] J.A. Weil, J.R. Bolton, and J.E. Wertz. *Electron Paramagnetic Resonance: Elementary Theory and Practical Applications*. Wiley, 1994.

[28] A. Lund, S. Shimada, and M. Shiotani. *Principles and Applications of ESR Spectroscopy.* Principles and Applications of ESR Spectroscopy. Springer, 2011.

[29] Stanford Research. *Model SR830 RF Lock-In Amplifier.*

[30] J Cottom, G Gruber, P Hadley, M Koch, G Pobegen, T Aichinger, and A Shluger. Recombination centers in 4H-SiC investigated by electrically detected magnetic resonance and ab initio modeling. *Journal of Applied Physics*, 119(18):181507, 2016.

[31] Alexander Schnegg, Jan Behrends, Matthias Fehr, and Klaus Lips. Pulsed electrically detected magnetic resonance for thin film silicon and organic solar cells. *Phys. Chem. Chem. Phys.*, 14:14418–14438, 2012.

[32] Cheuk Chi Lo. *Electrical Detection of Spin-Dependent Transport in Silicon.* PhD thesis, University of California at Berkeley, 2011.

[33] Daniel J Lepine. Spin-dependent recombination on silicon surface. *Physical Review B*, 6(2):436, 1972.

[34] We Shockley and WT Read Jr. Statistics of the recombinations of holes and electrons. *Physical review*, 87(5):835, 1952.

[35] D Kaplan, I Solomon, and NF Mott. Explanation of the large spin-dependent recombination effect in semiconductors. *Journal de Physique Lettres*, 39(4):51–54, 1978.

[36] AV Barabanov, OV Tretiak, and VA L'vov. Complete theoretical analysis of the Kaplan-Solomon-Mott mechanism of spin-dependent recombination in semiconductors. *Physical Review B*, 54(4):2571, 1996.

[37] MA Jupina and PM Lenahan. A spin dependent recombination study of radiation induced defects at and near the Si/SiO2 interface. *IEEE Transactions on Nuclear Science*, 36(6):1800–1807, 1989.

[38] BC Bittel, PM Lenahan, JT Ryan, J Fronheiser, and AJ Lelis. Spin dependent charge pumping: A new tool for reliability studies. In *2011 IEEE International Integrated Reliability Workshop Final Report*, 2011.

[39] Thomas Aichinger and Michael Nelhiebel. *Characterization of MOSFET Interface States Using the Charge Pumping Technique*, pages 231–255. Springer International Publishing, Cham, 2015.

[40] Alberto Salinaro. *Characterization and Development of the 4H-SiC/SiO2 Interface for Power MOSFET Applications.* PhD thesis, Friedrich-Alexander-Universität Erlangen-Nürnberg, 2015.

[41] T. Grasser. *Hot Carrier Degradation in Semiconductor Devices.* EBL-Schweitzer. Springer International Publishing, 2014.

[42] Nguyen Tien Son, Xuan Thang Trinh, LS Løvlie, BG Svensson, K Kawahara, J Suda, T Kimoto, T Umeda, J Isoya, T Makino, et al. Negative-u system of carbon vacancy in 4H-SiC. *Physical review letters*, 109(18):187603, 2012.

[43] V Lang, CC Lo, RE George, SA Lyon, J Bokor, T Schenkel, A Ardavan, and JJL Morton. Electrically detected magnetic resonance in a W-band microwave cavity. *Review of Scientific Instruments*, 82(3):034704, 2011.

Appendices

Appendix A

Setup

In order to reach cryogenic temperatures during an EDMR measurements some parts had to be built in the workshop. As explained in section 2.1 the liquid nitrogen (LN_2) dewar was connected to the cavity over double walled glass tubes. The sample holder was introduced from the top. Different views on the setup and the built parts are shown in figure A.1. The plans of the parts that were built in the workshop can be found on page 60. The adaptor on top of the cavity was made out of aluminium, since it had to be a non-magnetic material. This part is marked as Bauteil 1 in the plan. It was built with a brass screw on the top, which had the purpose to fix the steel cylinder that held the sample holders. The steel cylinder is marked as Bauteil 2 in the plans. it hat a 2 mm wide and a 5 mm deep slit on the top. Due to brass screw it was possible to change the angle of the cylinder and therefore the angle of the sample holder with respect to the magnetic field. In order to ensure a good thermal insulation between the cavity and the aluminium adaptor both were separated by a Teflon ring which is marked as Bauteil 3 in the plans. The alignment of these parts in the setup can be seen in figure A.1. The purpose of the adaptor was to avoid any freezing of the electrical contacts on the sample holder. Due to the height of the aluminium adaptor there was a sufficient temperature gradient. The temperature at the contacts was not low enough to cause the water in the air to freeze.

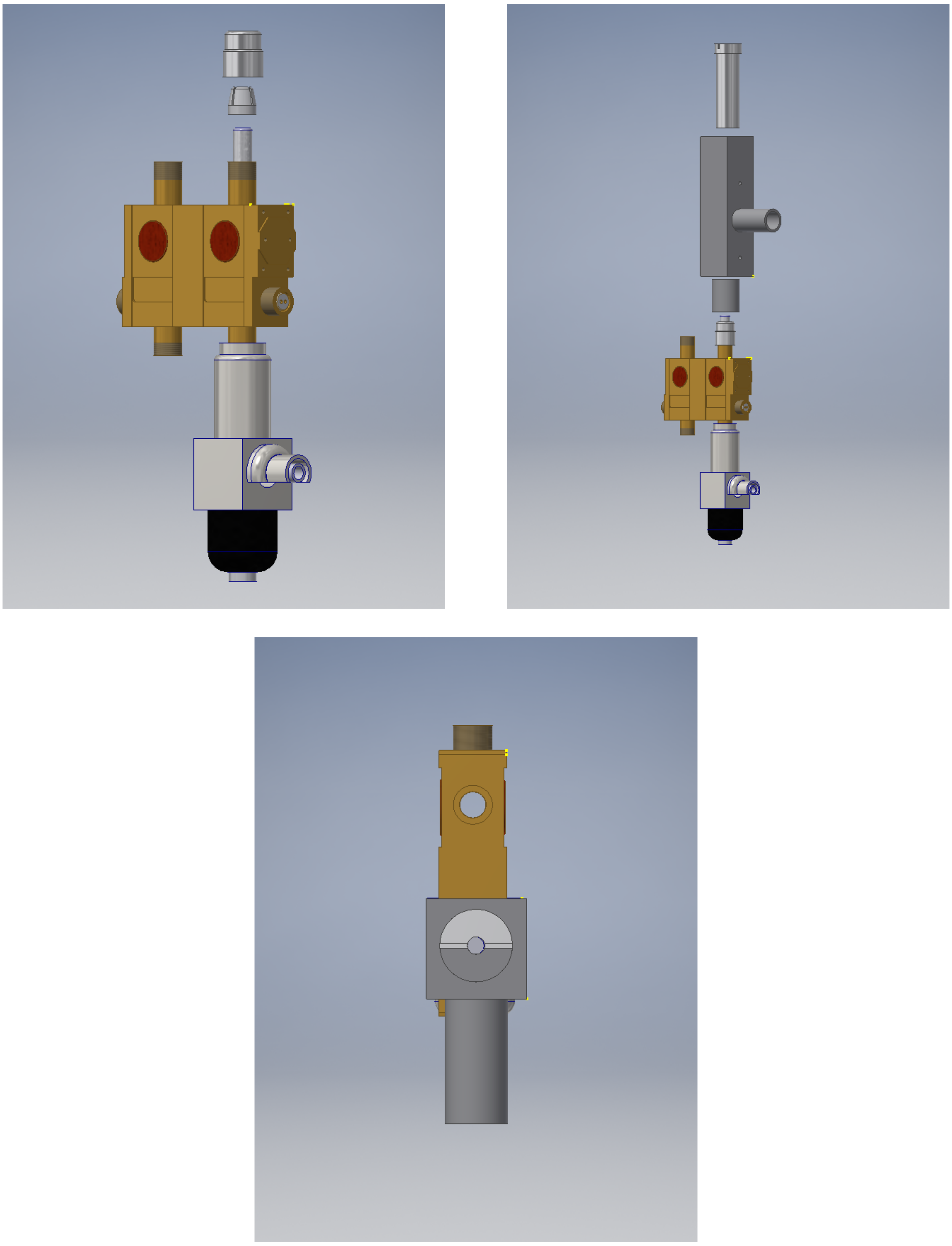

Figure A.1: 3D-model of the microwave cavity (gold) and the adaptors that were built in the workshop.

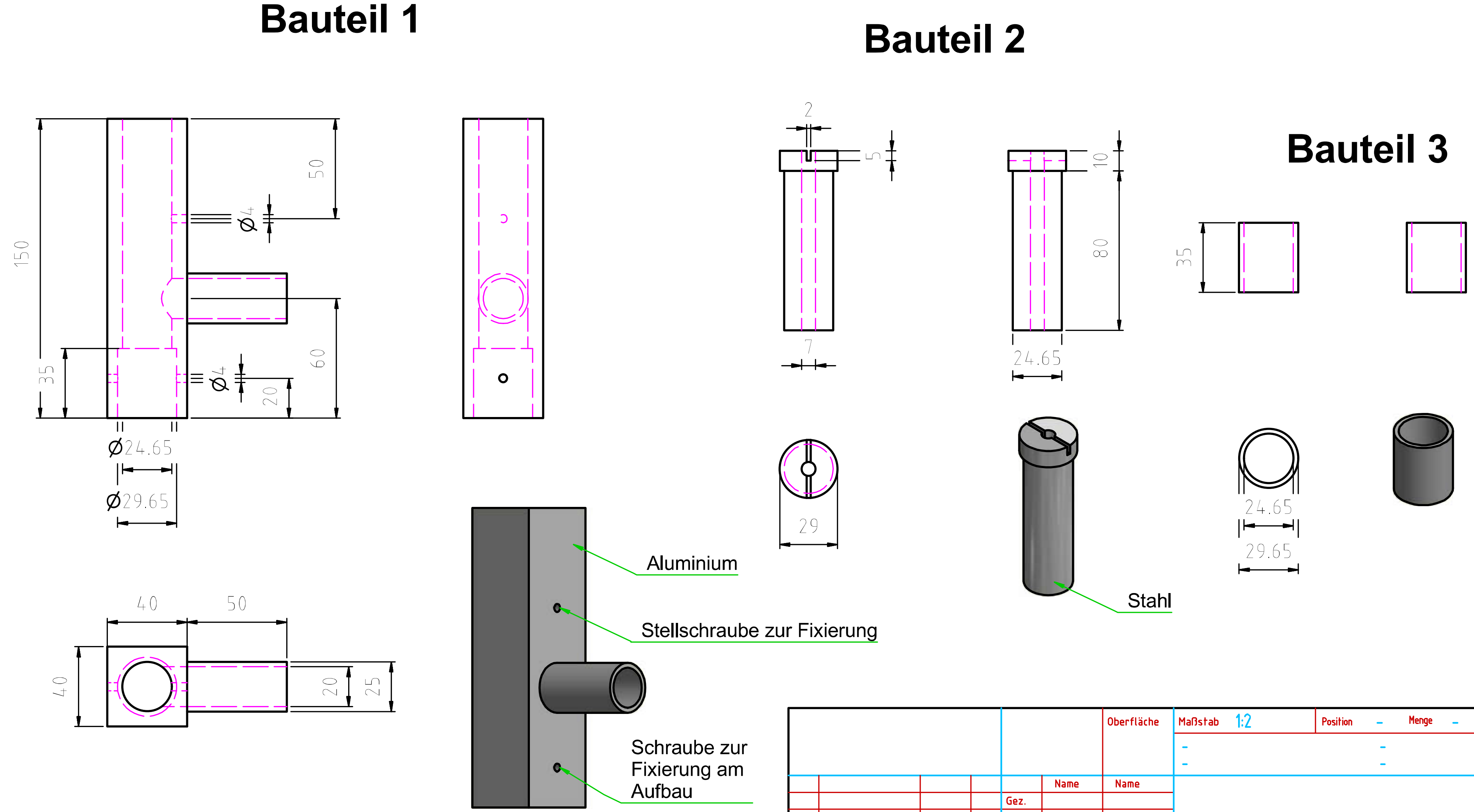

Oberfläche	Maßstab 1:2	Position -	Menge -
	- -		- -
	Name	Name	Bauteile für den ESR Aufbau
Gez.			
Geprüft			
Norm			
			-
			Blatt -
			Bl

Status	Änderungen	Name	Name	Dateiname